

A HIGH SIGNAL-TO-NOISE RATIO COMPOSITE SPECTRUM OF GAMMA-RAY BURST AFTERGLOWS

L. CHRISTENSEN¹, J. P. U. FYNBO², J. X. PROCHASKA³, C. C. THÖNE⁴, A. DE UGARTE POSTIGO⁴, P. JAKOBSSON⁵*Draft version November 19, 2010*

ABSTRACT

We present a composite spectrum of 60 long duration gamma-ray burst (GRB) afterglows with redshifts in the range $0.35 < z < 6.7$ observed with low resolution optical spectra. The composite spectrum covers the wavelength range 700–6600 Å in the rest frame and has a mean signal-to-noise ratio of 150 per 1 Å pixel and reaches a maximum of ~ 300 in the range 2500–3500 Å. Equivalent widths are measured from metal absorption lines from the Ly α line to ~ 5200 Å, and associated metal and hydrogen lines are identified between the Lyman break and Ly α line. The average transmission within the Lyman forest is consistent with that found along quasar lines of sight. We find a temporal variation in fine-structure lines when dividing the sample into bursts observed within 2 hours from their trigger and those observed later. Other lines in the predominantly neutral gas show variations too, but this is most likely a random effect caused by weighting of individual strong absorption lines and which mimics a temporal variation. Bursts characterized with high or low prompt GRB energy release produce afterglows with similar absorption line strengths, and likewise for bursts with bright or faint optical afterglows. Bursts defined as dark from their optical to X-ray spectral index have stronger absorption lines relative to the optically bright bursts. The composite spectrum has strong Ca II and Mg II absorption lines as commonly found in dusty galaxies, however, we find no evidence for dust or a significant molecular content based on the non-detection of diffuse interstellar bands. Compared to starburst galaxy spectra, the GRB composite has much stronger fine-structure lines, while metal absorption lines are weaker.

Subject headings: Galaxies: high-redshift gamma rays: bursts

1. INTRODUCTION

Optical spectra of long duration gamma-ray burst (GRB) afterglows provide a means to study the physical condition of the interstellar medium in their host galaxies through the associated metal absorption lines. While the host galaxies themselves are generally too faint to allow for detailed spectroscopic studies, spectra of the afterglows obtained shortly after the burst can achieve much higher signals. High resolution spectra of individual bursts have shown that GRBs reside in galaxies with large gas column densities and sub-solar metallicities (Vreeswijk et al. 2004; Chen et al. 2005). Host galaxy abundance ratios and metallicities have been measured (Savaglio et al. 2003; Vreeswijk et al. 2006), and evidence for galaxy outflows has been established from the presence of multiple absorption components separated in velocity space (Schaefer et al. 2003) and from correlation of absorption line species with host galaxy luminosity (Chen et al. 2009). The distances from the burst site to the absorbing material has been determined to be larger than a few tens of pc (Dessauges-Zavadsky et al. 2006; Prochaska et al. 2006; Chen et al. 2007; D’Elia et al.

2010), while in other cases the time variations of fine-structure lines (Vreeswijk et al. 2007; D’Elia et al. 2009a; Ledoux et al. 2009), or the presence of vibrationally excited H₂ molecules (Sheffer et al. 2009) indicated a distance of 0.4–2 kpc. While this is in itself interesting for the study of the nature and physical conditions present in high redshift star forming galaxies, one of the goals of afterglow absorption line studies is to constrain the nature of the progenitor of the GRB, but the diverse properties of GRB afterglows have made this difficult.

At the average burst redshift of $\langle z \rangle \sim 2.2$ (Jakobsson et al. 2006b, see also Web site⁶ with an updated sample) observed with the *Swift* satellite (Gehrels et al. 2004), the rest-frame UV spectra reveal that GRBs occur in galaxies which contain large amounts of neutral gas. Generally, the hydrogen column density determined from the GRB spectra lie in the damped Lyman- α (DLA) regime $\log(N(\text{H I})/\text{cm}^{-2}) > 20.3$, and both hydrogen and metal column densities are typically larger than observed in intervening DLAs towards quasars (Savaglio et al. 2003; Jakobsson et al. 2006a). Quasar sight lines with DLAs intersect and probe the interstellar environment of a galaxy at an impact parameter which is typically less than 10 kpc (e.g., Møller et al. 2002, 2004), although some candidates DLA galaxies are found at even larger impact parameters (Christensen et al. 2007) in the outskirts of the galaxies. In contrast, long duration GRBs explode in young star forming galaxies (e.g., Christensen et al. 2004), and are located close to the most luminous region in the host (Bloom et al. 2002; Fruchter et al. 2006; Svensson et al. 2010). The difference between the two

¹ Excellence Cluster Universe, Technische Universität München, Boltzmanstrasse 2, 85748 Garching, Germany; lise.christensen@ph.tum.de

² Dark Cosmology Centre, Niels Bohr Institute, University of Copenhagen, Juliane Maries Vej 30, 2100 Copenhagen Ø, Denmark

³ Department of Astronomy and Astrophysics, UCO/Lick Observatory, University of California, 1156 High Street, Santa Cruz, CA 95064, USA

⁴ INAF - Osservatorio Astronomico di Brera, via E. Bianchi 46, 23807, Merate, Lc, Italy

⁵ Centre for Astrophysics and Cosmology, Science Institute, University of Iceland, Dunhagi 5, IS-107 Reykjavik, Iceland

⁶ <http://www.raunvis.hi.is/~pja/GRBsample.html>

samples can be described by the diversity in impact parameters (Prochaska et al. 2007b; Fynbo et al. 2008; Pontzen et al. 2010).

While high spectral resolution studies can reveal the impact on the environment near the GRB event, low spectral resolution studies obtained for fainter afterglows also provide valuable information. However, significant discrepancies have been found between GRB afterglows where high resolution spectra seem to indicate lower metallicities than the afterglows observed with lower resolution (Ledoux et al. 2009), although the effects or biases which cause this discrepancy are not understood.

The current knowledge of the interstellar medium (ISM) in GRB host galaxies relies on a few well studied afterglows at a range of redshifts. Additional knowledge can be gained by taking advantage of a large set of GRB afterglows at different redshifts which sample different rest-frame wavelengths. By creating a composite spectrum, we can study the typical properties in a high quality spectrum over a large rest-frame wavelength range. Here we present a composite spectrum of 60 GRB afterglows from the largest sample which has been analyzed in a consistent manner (Fynbo et al. 2009, 2010). The composite spectrum allows us to measure which lines are typically present in a GRB afterglow and their average equivalent widths and metallicities.

This paper is organized as follows. In Sect. 2 we explain the benefits and limitations for the physical interpretation of the composite afterglow spectrum. We describe the full sample and how the composite spectrum is created in Sect. 3. In Sect. 4 the global properties are investigated and the list of absorption lines is presented, while in Sect. 5 we investigate specific absorption lines in detail. In Sect. 6 the absorption line strengths are compared with other high redshift galaxies. Metallicities are derived in Sect. 7. We discuss the results and potential bias effects in the interpretation of the composite spectrum as well as future prospects in Sect. 8.

2. MOTIVATION FOR CONSTRUCTING A COMPOSITE SPECTRUM

The goal of this study is to use a unique database of low-resolution spectra to explore whether fainter lines are detectable when combining all spectra compared to detections in individual, lower signal-to-noise (S/N) spectra. Since all afterglow spectra seem to be unique, we also want to explore specific absorption line features and their possible dependence on global properties for the GRB explosion. A detailed investigation of the variations of each detected absorption line in the set of spectra will be presented in a forthcoming paper (A. de Ugarte Postigo et al., 2011, in preparation).

A potential benefit of having a high signal-to-noise ratio afterglow composite spectrum which covers a large rest-frame wavelength range is to compare existing or future individual low-resolution afterglow spectra to answer a set of questions: (i) Does the (new) optical afterglow spectrum have unusual absorption lines or ratios thereof? (ii) What absorption lines are detectable given the GRB redshift and the S/N of the data? (iii) Is it possible to derive redshift of a very noisy afterglow spectrum by convolving it with the composite spectrum?

Certain limitations exist for the analysis of a composite spectrum too, where some quantities are better explored

with high resolution optical spectra. First, the velocity spreads of individual absorption lines are not possible to analyze at low spectral resolution. Second, some lines may be particularly blended with other lines, for example molecular H_2 lines which fall in the $Ly\alpha$ forest. In addition, iron fine-structure lines are affected by blending in the low resolution data, so a detailed analysis of their temporal variations has to use higher spectral resolution data.

Individual afterglows have shown a wide range of metallicities in GRB hosts, and the composite is biased towards the brightest afterglows in the full sample as explained in Sect. 3. However, with this in mind we can use the wide rest-frame wavelength coverage of the composite spectrum combined with the detection of a large number of weak absorption lines, to derive the average column density of a large number of metal species in Sect. 7. This presents a unique possibility for the study of the interstellar medium (ISM) in faint, high redshift galaxies, although the diversity of metallicities probed by GRBs have to be investigated using individual higher resolution spectra.

3. AFTERGLOW SAMPLE

The largest systematic analysis of low resolution optical spectra of long duration GRB afterglows performed to date is presented in Fynbo et al. (2009, hereafter F09). While the majority of spectra in F09 involves low-resolution spectra, they also include five high resolution spectra observed either with UVES on the VLT or HIRES at the Keck Telescope. To date, optical spectra of GRB afterglows are mostly obtained at low resolution because afterglows are typically faint ($R > 20$ mag) at the time of the start of the observations. The low spectral resolution data from the sample in F09 provide the basis for this present follow-up study.

3.1. Sample selection

The aim of the sample selection is to construct a sample of long GRBs that is selected independent of the optical properties of the afterglows and at the same time has as high completeness in high quality optical follow-up as possible.

To get a well selected sample which is independent of the optical properties of the afterglow, and to achieve a high degree of completeness and good quality optical spectra, a set of selection criteria was used according to the methods described in Jakobsson et al. (2006b): (i) the burst duration is longer than 2 sec., (ii) accurate localization obtained with X-ray observations, (iii) small foreground Galactic extinction ($A_V \leq 0.5$ mag) in the direction of the burst, (iv) declination useful ($-70^\circ < \delta < +70^\circ$) for optical follow up observations, and finally (v) a solar distance greater than 55° at the time of the GRB. A total number of 146 *Swift* bursts observed between March 2005 and September 2008 fulfill these criteria, and optical spectra have been obtained for 69 of these (see F09 for details on each individual object).

From the full sample of spectra, we here focus on the 66 afterglows which were observed with low-resolution optical spectroscopy using the following instruments: FORS1 and FORS2 on the VLT, ALFOSC on the Nordic Optical Telescope, GMOS-N and GMOS-S on the Gemini North and South, respectively, and finally LRIS on the Keck

Telescope. Depending on the grating or grism chosen for the observations, these instruments provided spectra with resolutions between 315 and 2140. We exclude afterglow spectra with uncertain redshift determination due to the lack of absorption lines in their spectra, and where the redshifts were determined from photometric redshift methods from their host galaxies. We also exclude afterglow spectra where only upper limits on the redshifts have been established. In total 60 afterglow spectra pass these criteria and were used to create the composite spectrum. Their redshifts lie in the range $0.35 < z < 6.7$, with a mean of $z = 2.22$.

Given the variety of instruments used, time after the trigger for the spectroscopic observations following the burst, and intrinsic magnitude of the afterglow, the S/N of the individual spectra vary between a few and ~ 200 for the burst with the highest signal (GRB 060729 at $z = 0.5428$).

For the $z \gtrsim 2$ GRBs, F09 determine their neutral hydrogen column densities to lie in the range $17.0 < \log(N(\text{H I})/\text{cm}^{-2}) < 22.7$, and most of them are in the DLA regime. Metallicities have been determined for a subsample of afterglows which give typical values between 1% and 30% solar (Watson et al. 2006; Fynbo et al. 2006; Prochaska et al. 2007b; Fox et al. 2008; Elíasdóttir et al. 2009; Prochaska et al. 2009). The associated metal absorption lines are typically very strong and are certain to be associated with the host galaxy itself.

Although the observational biases for the sample as a whole are well known (F09), the effects on the composite spectrum can be severe. For example, dust obscuration will render the afterglow fainter, and the S/N will typically be lower. Bursts which are observed early, have low extinction, lie at lower redshifts, occur in a certain environment, or also possibly in an environment with a specific chemical composition at a fortuitous distance from the burst, are more likely to have a bright afterglow. Because of the weighting scheme for creating the composite spectrum these bursts will dominate over the remaining ones. Alternative combination schemes are found to produce a spectrum with a worse S/N and one with a smaller useful wavelength range, but general properties are found to be consistent, so this paper focuses mainly on the weighted combination scheme described below.

3.2. Composite spectrum

Each individual spectrum was normalized with a cubic spline function. The continuum level was estimated by fixing spline points in regions that were not contaminated with any absorption lines, either intrinsic to the GRB or from intervening systems as listed in the tables in F09, or from the atmosphere. The regions for the continuum was estimated by eye, and special care was taken in the wavelength regions around and blueward of the Ly α line. This manual procedure was estimated to be most appropriate since the individual spectra have widely different quality and spectral range, so that an automatic procedure would be very complicated. Since the normalization was done by eye, the errors introduced on a pixel-by-pixel scale are not known, so we cannot propagate the error from the normalization procedure throughout. With iterations of the normalization, we estimate from the spectra with the best signal that we can achieve an accuracy

better than 1% for the normalization. Whenever possible, we used the flux calibrated afterglow spectra to derive the normalized spectra, because these should follow a pure power law. For 15 of the 60 spectra, we did not have a flux calibrated spectrum, while other flux calibrated spectra had artificial features introduced by errors in the flux calibration from the spectrophotometric star as mentioned in F09. These features were removed too by the normalization.

The associated error spectra were normalized as well using the same spline function. GRB afterglows can have different spectral slopes, so the normalization was a necessary step before the composite spectrum is computed. Any specific signature of the GRB environment such as dust extinction, and the 2175 Å bump that appeared for example in the GRB 070802 afterglow (Krühler et al. 2008; Elíasdóttir et al. 2009), is eliminated during this process. Here we do not aim to analyze the composite, line of sight averaged, extinction curve.

Before combining the spectra, we masked absorption features that were unrelated to the GRB environments. To avoid contamination by absorption lines from intervening absorption systems, we masked each of the detected lines arising in intervening systems which were not associated with the GRB (see Tables 5–72 in F09). We masked fringes present at red wavelengths in ALFOSC spectra, and fringes present at wavelengths larger than 7000 Å in spectra obtained with the blue sensitive FORS1 detector installed in April 2007. We also masked atmospheric features such as the strong telluric bands around 6900, and 7600 Å, but also weaker telluric bands around 6300, 7200, 8200, and 9000 Å were masked; if not, they would introduce artifacts and spurious absorption lines redward of 3000 Å in the rest frame. The masking was done by assigning a large value (10^6) to the error spectrum at the corresponding wavelengths.

The typical dispersion obtained with the FORS V300 grating is $3.25 \text{ Å pixel}^{-1}$ and the average redshift of all the bursts which contribute to the composite is $z = 2.22$. The average redshift therefore matches the dispersion of the low resolution perfectly $\lambda_{\text{rest}} = \lambda_{\text{obs}}/(1+z)$, so the optimal choice is to shift each spectrum to $z = 0$ with a dispersion of 1 Å pixel^{-1} . We investigated the outcome of the composite spectrum by choosing other resampling sizes for the dispersion, e.g., 0.5 and 0.8 Å pixel^{-1} , however, the absorption lines were not better resolved and the S/N decreased correspondingly. We adopted the redshift for each GRB from neutral species associated with the GRB environment as listed in the tables in F09.

The spectra were combined using the weighted average

$$f_{\lambda, \text{comb}} = \sum_i (f_{i, \lambda} / \sigma_{i, \lambda}^2) / \sum_i 1 / \sigma_{i, \lambda}^2 \quad (1)$$

where the flux f at each wavelength λ was weighted by its error σ , and summed over all spectra, i . The associated error spectrum was also calculated:

$$\sigma_{f, \lambda, \text{comb}}^2 = \left(\sum_i 1 / \sigma_{i, \lambda}^2 \right)^{-1}. \quad (2)$$

The resulting composite spectrum and its error spectrum is shown in Fig. 1, and Table 1 lists the relative fluxes and uncertainties. The median value of the error spectrum is 0.0065 from 1000–2000 Å, corresponding to a median S/N = 150. At wavelengths 2000–3500 Å

the error is smaller, and the $S/N = 250\text{--}300$ per \AA , as illustrated in the middle sub-panels in Fig. 1. At wavelengths larger than 3500 \AA the S/N depends on the exact region, where only few, low signal data contribute, and where some regions have lower signal because the input spectra receive a low weight in regions of strong telluric absorption lines. Only one low redshift afterglow (GRB 061021 at $z = 0.3463$) contributes to the composite beyond 5800 \AA , and here the noise is significantly larger than in other spectral bins.

Apart from the regular error spectrum there are other effects that add to the noise. The composite spectrum is affected by uncertainties from the normalization of the individual spectra. If this is not done correctly, we can artificially introduce absorption lines in the composite. At the very high S/N level, it is necessary that the normalization is done to a level better than $0.5\text{--}1\%$, otherwise features which resemble absorption lines will be introduced to the composite spectrum artificially and the uncertainty will introduce systematic errors for the equivalent widths. The normalization is particularly important for the individual spectra with good S/N which dominate the composites, however, when the S/N is good, the continuum flux level is also easier to identify visually.

As afterglow spectra show a range of abundances and equivalent widths for individual absorption lines, it is interesting to determine the spreads of values with wavelength. We examined the variance of values from the sub-set of the 60 spectra that went into each wavelength bin. This variance spectrum essentially shows a flat behavior with a value around $0.05\text{--}0.1$ from $1000\text{--}4000 \text{ \AA}$, while redward of 4000 \AA it has a larger scatter of values between 0 and 0.5 . The reason why the variance spectrum does not have a larger value at the location of the metal absorption lines is likely because many of the individual spectra have low S/N , so they will dominate the spreads of values. One exception exists at the $\text{Ly}\alpha$ line around $1216\text{--}1230 \text{ \AA}$, where the variance is larger ($0.3\text{--}0.4$) because of the large range of hydrogen column densities probed by individual GRBs.

A few individual high S/N spectra will necessarily dominate the composite spectrum. In order to check for systematic effects we also created a simple median spectrum, again masking out intervening absorption systems as well as atmospheric absorption lines. The median spectrum has a lower $S/N \sim 50$, estimated by the standard deviation in regions free of absorption lines, and a useful spectral range between $1000\text{--}2700 \text{ \AA}$.

In addition to this, we also investigated the output where the spectra were multiplied with each other and divided by the number of systems. In practical terms, the spectra were added in logarithmic space, while omitting the masked pixels.

$$\log(f_{\lambda,\text{comb}}) = \Sigma_i \log(f_{i,\lambda})/N_\lambda, \quad (3)$$

where N_λ is the number of spectra which contributes to each wavelength bin. Without the normalization, the composite spectrum will be completely dominated by absorption lines, and have a very low output S/N .

Physically, this method corresponds to placing the absorbing systems one after the other along the line of sight, and then taking the average. In this case we avoid the

systematic effects from weighting the individual spectra, however, we are again limited by the resulting S/N which is also $\lesssim 50$. This implies that many of the faintest absorption lines are lost in the noise.

4. RESULTS

Unless specifically mentioned, the following sections involves the weighted combination of the 60 afterglows, because we found that the general results did not depend on which of the three combination methods we used. The largest amount of information was therefore obtained with the highest S/N spectrum with the largest rest-frame wavelength coverage. Some results were also derived by creating sub samples from the full sample of bursts.

4.1. Absorption line list

Compared to individual spectra, we see significantly more absorption lines in the composite. Even the high resolution afterglow spectra obtained, e.g., with UVES or HIRES, are not able to detect some of the fainter lines at a high significance; although high resolution spectra are better suited to investigate lines (e.g., Ledoux et al. 2009) which are blended at the lower resolution.

Table 2 lists all the lines and rest-frame equivalent widths (W_r) detected at above the 3σ uncertainty level. Among all the lines identified, we checked if there are any missing lines that should be detectable. From the singly ionized species which are the dominant ionization state, we only find three non-detections, all of which are expected to be very weak. The non-detection of $\text{Ni II } \lambda 1502$, $\text{Co II } \lambda 1466$, and $\text{Cr II } \lambda 2040$ are therefore not surprising. Some afterglow spectra have unidentified absorption lines, as several ones in F09 do. After a careful masking of telluric features in the individual spectra, the composite spectrum does not appear to have any unidentified lines. Other very weak absorption lines which were uniquely detected in the GRB 080607 spectrum, such as $\text{O I } \lambda 1355$, $\text{Mg I } \lambda 1683$, $\text{Co II } \lambda 1574$ and $\text{Ge II } \lambda 1602$ (Prochaska et al. 2009), are not recovered in the composite spectrum.

Identified lines which have rest-frame wavelengths separated by $2\text{--}5 \text{ \AA}$ were deblended by fitting Gaussian functions to the blends of lines using the `splot` routine in IRAF, keeping the wavelengths of the lines fixed, and fitting a single absorption line width. This routine also estimated the uncertainties using a representative value from the composite uncertainty spectrum around the line blend to represent the pixel statistics. Lines closer together than $\sim 2 \text{ \AA}$ were not deblended and here the total W_r is listed. Reference rest-frame wavelengths for the transitions were found in the atomic table in Morton (2003). The W_r uncertainties do not include the uncertainty for the placement of the continuum.

Since some spectra with high S/N dominate the composite, we compared with the median composite and the multiplied spectra. Although their overall S/N are lower, we still find the same absorption lines in the three composites and the W_r of the strong absorption lines are consistent to within the errors.

To check further whether some of the weaker lines are randomly caused by errors in the normalization of the individual spectra, we created two independent composites. The spectra were sorted according to their S/N , and

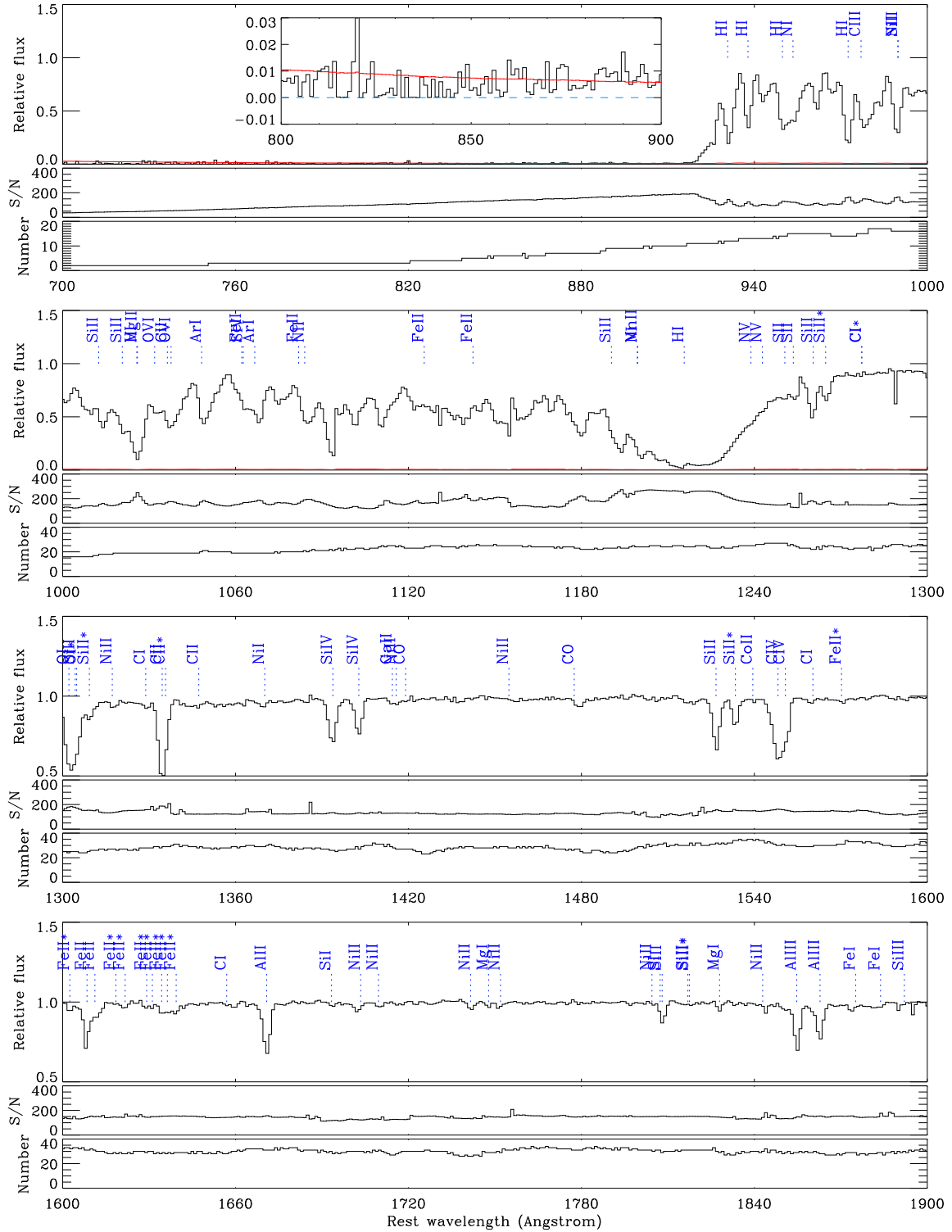
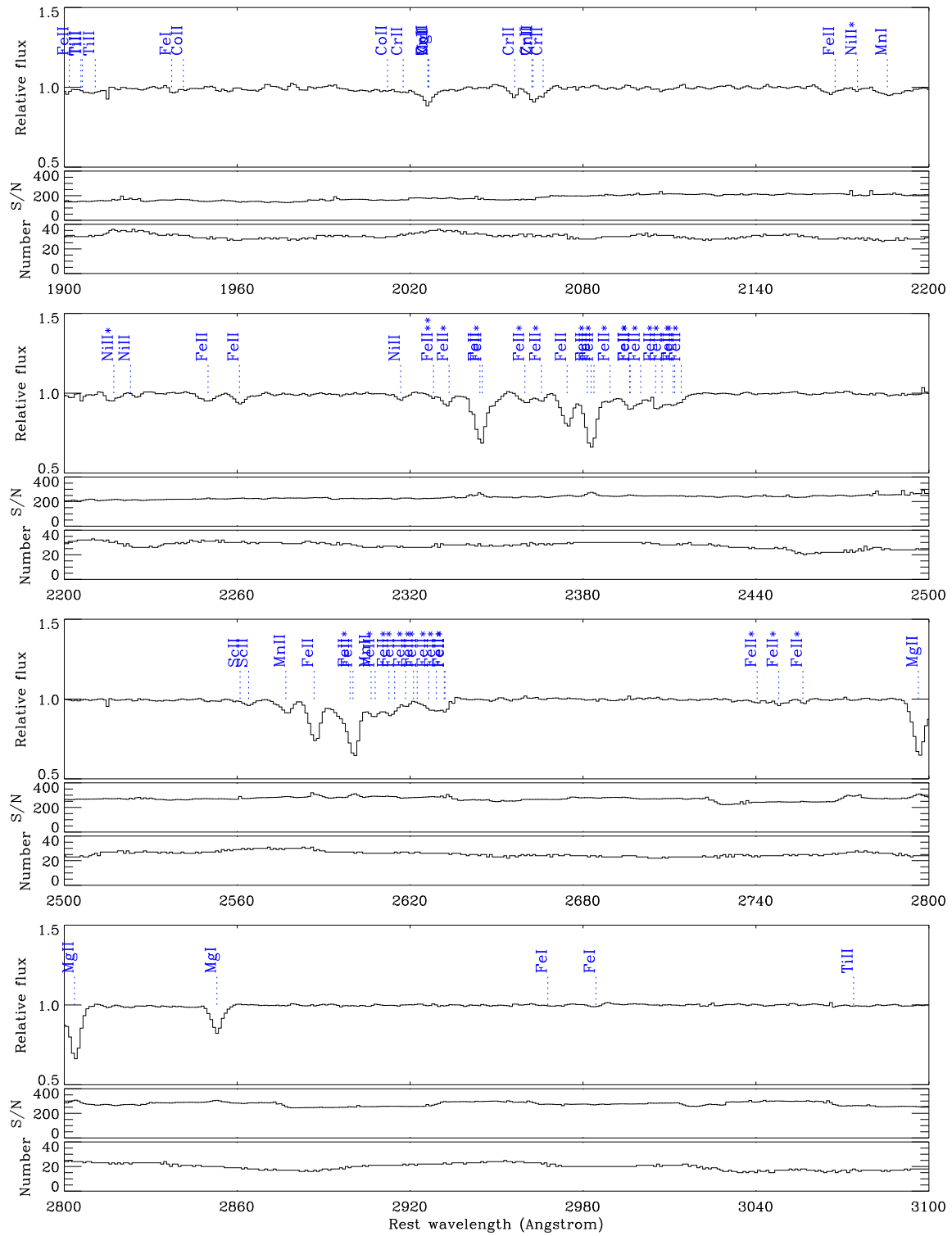
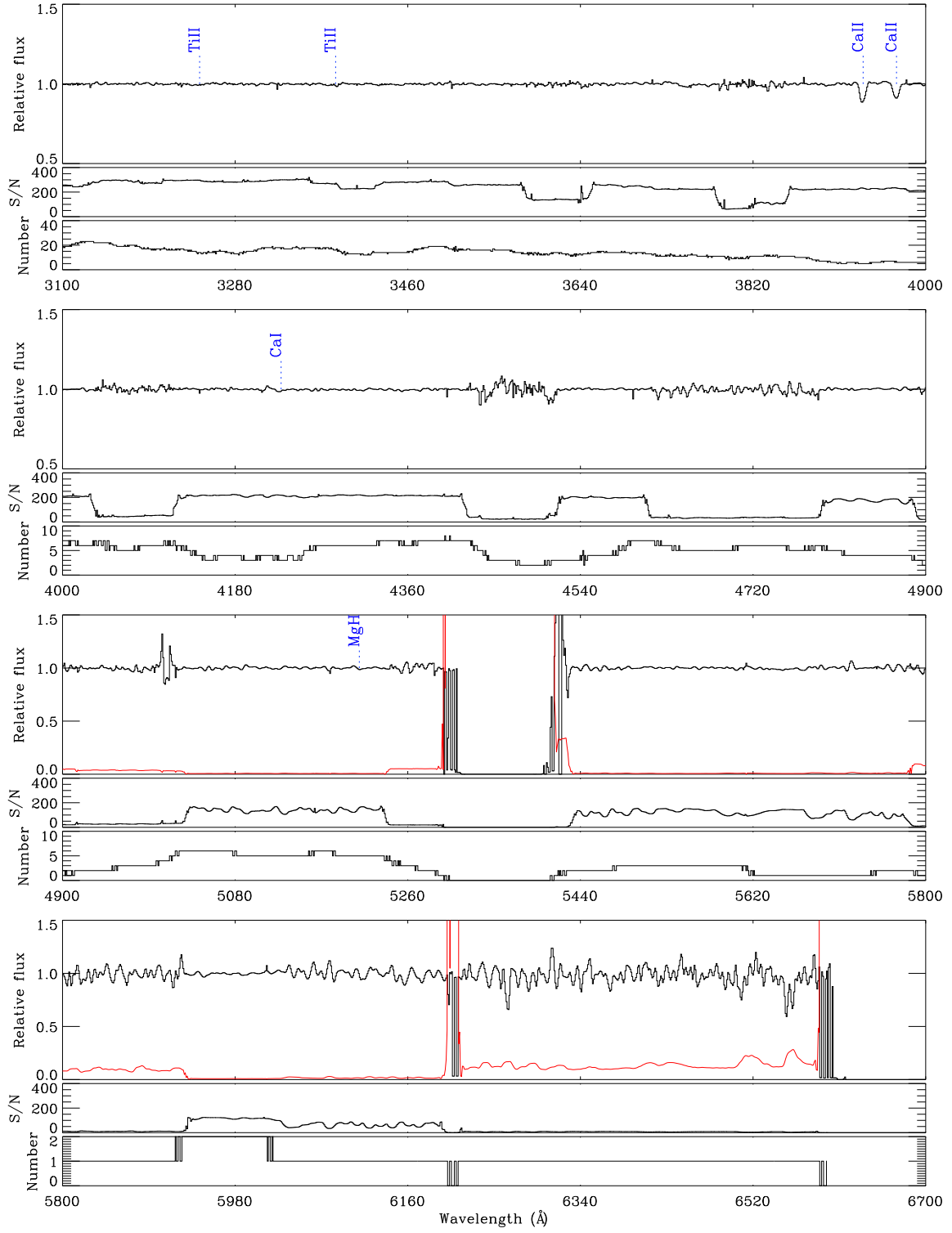


FIG. 1.— Each sub-spectrum consists of three parts. *Top*: The composite spectrum and its associated error spectrum (red line) which typically has a value around 0.005. *Middle*: The corresponding S/N per pixel, and the *Bottom*: shows the number of afterglow spectra that are used in the composite per spectral pixel. All detected absorption lines from Tables 2 and 3 are indicated. Note the change of scale on the y-axis, which implies that the error spectrum is not always visible.

FIG. 1.— *Continued.*

FIG. 1.— *Continued.*

two subsets of composite spectra with the same S/N were created. Since the GRBs have different redshifts, the best method would be to make two composites with a similar S/N ratio throughout the spectral range, and with a similar redshift distribution so that there are an equal number of objects contributing to each spectral pixel. This is not feasible in practice, so the spectra were simply combined according to their S/N ratio, and the two spectra have almost the same average redshift $z = 2.4$ and $z = 2.0$, respectively. We checked whether the absorption lines found in the full composite spectrum are present in both of the sub composites. This is not always the case, as noted in the comments to Table 2. We cannot rule out that the lines are not real based on this test; the absorption lines may potentially be present in very few lines of sight, but randomly one that was observed at a high S/N. Additionally, the presence or absence of the absorption lines can be due to temporal variations as discussed in Sect. 4.4. In particular, some lines appear quite strong in one composite, but are absent in the other composite spectrum.

Due to the wide range of $N(\text{H I})$ column densities, the Ly α absorption line does not have a purely damped line profile, and residual emission can be seen in the Ly α trough. Nevertheless, the average value of $\log N(\text{H I}) = 22.0$ provides a good Voigt profile fit to the red wing of the line in the composite spectrum. At this high column density, the red wing of the absorption line extends to 1400 Å which is consistent with the theoretical line profile. It also affects the continuum estimate of the metal absorption lines in this wavelength range.

Blueward of the DLA, a mixture of metal absorption lines and intervening hydrogen absorption lines are present. Hence, measurements of the equivalent widths of lines in this region are likely to be contaminated by intervening H I clouds. Identified lines with wavelengths < 1215 Å are listed in Table 3.

As a consequence of the low resolution of the spectra, we see no evidence for any velocity shift of the absorption lines relative to each other or multiple components of individual lines as reported in studies of individual afterglows observed with higher resolution spectroscopy (e.g., Møller et al. 2002; Fiore et al. 2005; Chen et al. 2005; Prochaska et al. 2008b; Fox et al. 2008).

4.2. Ly α forest transmission

At $z \sim 2$, the intergalactic medium (IGM) expresses itself in quasar spectra as a series of H I Ly α transitions commonly termed the Ly α forest (Rauch 1998). In a single spectrum, the Ly α forest appears as a series of discrete absorption lines. If one considers an ensemble of sightlines, however, the stochastic nature of absorption produces an average, effective opacity τ_{eff} . Using high S/N spectra of bright quasars Dall’Aglio et al. (2008) fits the transmission in the Ly α forest as a function of redshift by the equation $T = e^{-\tau_{\text{eff}}}$ where $\tau_{\text{eff}} = 10^{-2.21 \pm 0.09} (1+z)^{3.04 \pm 0.17}$. In contrast to quasars which ionize their surroundings and create a proximity region with higher transmission nearby, GRBs and their hosts are expected to have relatively less impact on their surroundings, and the proximity effect will not be as pronounced. Therefore, GRBs are excellent probes of the transmission in the Ly α forest, in particular, in the view that they can be observed at extremely high redshifts

where the current record holder is GRB 090423 at $z = 8.2$ (Tanvir et al. 2009; Salvaterra et al. 2009).

At the average redshift of $z = 2.22$ for the composite spectrum, the expected transmission in the Ly α forest is $T = 0.8 \pm 0.1$. In the composite spectrum, many of the absorption lines in the Ly α forest are associated with the ISM in the GRB host galaxy (see Table 3). Without correcting for these lines, we find that the transmission is 0.6, but if we avoid the associated lines, the regions of the largest transmission where no metal absorption lines are expected suggests $T \sim 0.85$, as illustrated in the first two panels in Fig. 1. This is in excellent agreement with the prediction from the quasar transmission. Thus, we find no overall difference in the Ly α forest transmission towards GRBs and quasars. To analyze the forest and its evolution in further detail, one needs to look at higher spectral resolution data.

4.3. Lyman limit emission

The existence of the Ly α forest demonstrates that the IGM is predominantly ionized at $z < 6$. While quasars are known sources of ionizing radiation, they may not dominate the extragalactic UV background, especially at $z > 3$ (e.g., Faucher-Giguère et al. 2009). Instead, star-forming galaxies may contribute the majority of ionizing photons, but this requires that they have a non-negligible escape fraction f_{esc} . Since GRB hosts are potentially unbiased tracers of star formation they have been used as probes of the ionizing radiation escaping blueward of the Lyman limit into the IGM. The estimated escape fraction from the H I column density distribution function for GRB afterglows at $z > 2$ is $\langle f_{\text{esc}} \rangle = 0.02 \pm 0.02$ (Chen et al. 2007, ; F09). This value is consistent within the 1σ error with numerical simulations, which predict an escape fraction of 1% (Pontzen et al. 2010).

Blueward of the Lyman limit in the composite spectrum, we measure a relative flux level of 0.0060 ± 0.0050 in the wavelength range from 800 to 900 Å as illustrated in the small inserted panel in Fig. 1. At these rest-frame wavelengths, only 11 afterglow spectra contribute to the composite, and some only cover redward of 880 Å and have different S/N ratios in this wavelength range as listed in Table 4. Most afterglows at $z > 2$ have H I column densities in the DLA regime, where the escape of ionizing radiation is effectively blocked. Indeed, the average H I column density from the bursts in Table 4 is $10^{22.1 \pm 0.1} \text{ cm}^{-2}$, and at this high value the radiation blueward of the Lyman limit is completely absorbed.

The average redshift for those afterglow which contribute blueward of the Lyman limit is $z = 3.66$. At this redshift the average transmission in the Ly α forest is $T = 0.52$ (Dall’Aglio et al. 2008), and in the Ly β forest it is $T = 0.57$ (Madau 1995). Including these two transmission corrections, the measured relative flux blueward of the Lyman limit is $f = 0.020 \pm 0.017$, which is consistent with the values derived from the H I column density distribution.

Since clouds with column densities in the DLA regime effectively absorb all the Lyman limit photons, a significant escape fraction is only expected to be present for low column density systems. A few afterglows have revealed column densities well below the DLA limit, and GRB 050908 with $\log(N(\text{H I})/\text{cm}^{-2}) = 17.6 \pm 0.1$ has a significant level of ionizing radiation detected beyond the

Lyman limit ($f_{\text{esc}} = 13 \pm 4\%$), and appears to be a unique object among the whole sample. Because of the relatively low S/N for the GRB 050908 spectrum, eliminating it from the total composite changes flux blueward of the Lyman limit very little: $f = 0.018 \pm 0.017$. A couple of other systems observed with low resolution spectroscopy (GRB 060124, GRB 070411, and GRB 071020) have relatively low H I column densities, but their spectral ranges do not reach the Lyman limit. More studies which cover the very blue end of the spectral range are needed to determine the effects of the ionizing radiation from GRB host galaxies, and their impact on the extragalactic UV background radiation field.

4.4. Temporal variations

Our composite spectrum ignores the case of time variations in the fine structure levels. Several spectra show that the absorption lines strengths can change with time due to the temporal variation of the ionizing radiation from the central explosion (Dessauges-Zavadsky et al. 2006; Vreeswijk et al. 2007; D’Elia et al. 2009a; Ledoux et al. 2009).

The spectra included in this investigation are obtained at one particular time (Table 2 in F09) at an average of 3 hours after the burst in the rest frame for the composite spectrum. Since the spectra contribute to the composite weighted by their signal, the effective rest-frame observing time can be calculated by weighting according to a representative value for the S/N of each spectrum. This gives an effective observing time of $t_{\text{rest}} = 2.78$ hours after the burst in the rest frame for the composite spectrum. We investigate the cumulative effect of the observing time on the spectra, and look for temporal variations in absorption lines. We create two subsamples separated according to the time of the start of the spectroscopic observations after the burst trigger. The division takes into account the redshift of the GRB by shifting the start of the observing time to the rest frame. These sub-samples of composite spectra include 30 afterglow spectra obtained within 1.9 hours from the trigger (in the rest frame of the burst) which has an average redshift of $z = 2.4$, and 30 spectra obtained between 1.9 and 14 hours, which have an average redshift $z = 2.0$. Both composite spectra have a S/N between 100 and 200 in the wavelength range 1500–3500 Å. The magnitudes of the afterglows at the time of the trigger vary by ~ 4 mag in both the early and late-time samples, while the early sample is on average 1.4 mag brighter than the late sample (See Fig. 2 in F09).

A clear difference in the strength of the metal absorption lines is seen. Strong variations in the iron fine-structure lines are observed from the spectrum obtained at an average of 0.4 hours after the burst to that obtained 5 hours after the burst. However, also the species Fe II, Al III, Mg II, Zn II, Cr II, Ni II which trace the neutral gas seem to decrease in strength. In particular, the Fe II W_r decrease by a factor of 2–4 as illustrated in Fig. 2. Between the two composites, all the absorption lines appear to decrease in strength by a factor of ~ 2 . Other lines like C II, and Si II and the high ionization lines Si IV and C IV remain constant within 10–20% as illustrated in Fig. 3. The disappearing CO lines in Fig. 3 could also be ascribed to a temporal variation, but as explained in Sect. 5.3 the CO lines are only detected in the afterglows

from GRB 080607 and possibly also GRB 060210. Hence, it is not certain whether this is a real effect or just a coincidence from the strong CO lines in one GRB sight line. It is curious that GRB 080607 also has the earliest rest-frame observation time in the entire sample.

The simple median spectrum and the multiplied spectrum composites do not suffer from the possible biasing effects of weighting with noise level. Nevertheless, they also reveal changes in the absorption line strengths (both ground and excited states) between the early and the late time samples.

To date, no time series of individual afterglows have revealed any significant variations in the non-excited states. In particular, a time series of high resolution spectra of GRB 071031 showed constant high ionization lines (Fox et al. 2008). Therefore, we investigate whether other effects are at play in the composite spectra, and find the temporal changes of absorption line strengths to be a random effect caused by some afterglows with very strong absorption lines. In order to conclude this, we investigate $W_r^{\text{Mg II}}$ and $W_r^{\text{Fe II}}$ from individual systems as a function of the starting time for the spectroscopic observations as well as a function of redshifts as shown in Fig. 4. First, there are no systematic changes of the W_r with redshift. Second, there is a tendency that earlier observations have larger W_r , but including the measured W_r uncertainties any statistically significant correlation disappear. Both the early- and the late-time observations have spectra with high S/N ratio. Taking the W_r at face value in addition to the fact that the earlier observations have brighter afterglows and therefore give more weight to the composite, this mimics the behavior of a temporal variation of the composite spectrum. We therefore suspect that this effect is not physically real. A similar analysis of the C IV and Si IV W_r measurements and their S/N show a large scatter of values at all times, so the apparent constant value in the composites is also likely to be a random effect.

Apart from the composition of the external medium, the fine-structure line variations also depend on the input UV flux from the GRB. We investigated the effect by analyzing subsets of composites by separating according to the spectral slope β , derived from the power-law dependence of the flux $f_\nu \propto \nu^{-\beta}$. Values of β are listed for half of the bursts in Kann et al. (2010), while the remaining ones are obtained by fitting a power law to the flux calibrated spectra without including additional extinction. Including a set of possible extinction laws allows the spectral index a large range of values within the uncertainties. Here, we use the face values without including the uncertainties and create two subsamples separated at $\beta = 1$. Comparing the composite spectrum with lower β values (brighter UV than optical flux in f_λ units) with that obtained from afterglows with $\beta > 1$, we find that both have strong fine-structure lines, with no clear trend that one has systematically much stronger lines than the other. A more careful treatment of the spectral slope dependence would need to include systematic analyses including the uncertainties and the intrinsic extinction to derive the intrinsic UV flux from the afterglows. Such an analysis is beyond the scope of this paper.

4.5. Effect of GRB energy release

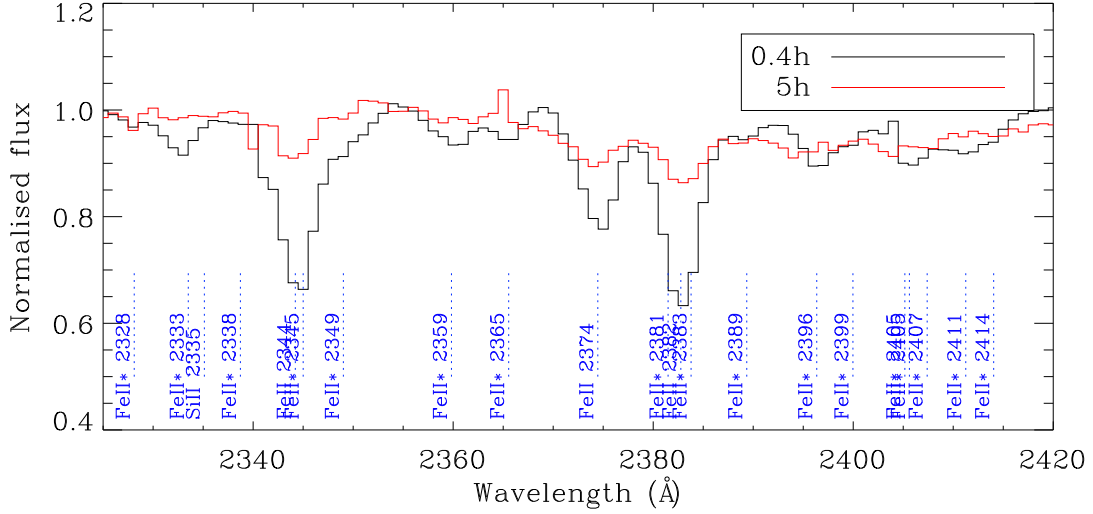


FIG. 2.— Apparent variation of the absorption line strength around the wavelength region where strong Fe II and Fe II* lines dominate. The spectra are labeled according to the average time for starting the spectroscopic observation after the trigger (0.4 and 5 hours, respectively). Strong variations of the fine structure lines are seen, but variations of the ground states (Fe II λ 2344, 2374, 2382) are most likely caused by the sampling of the spectra and is not physically real.

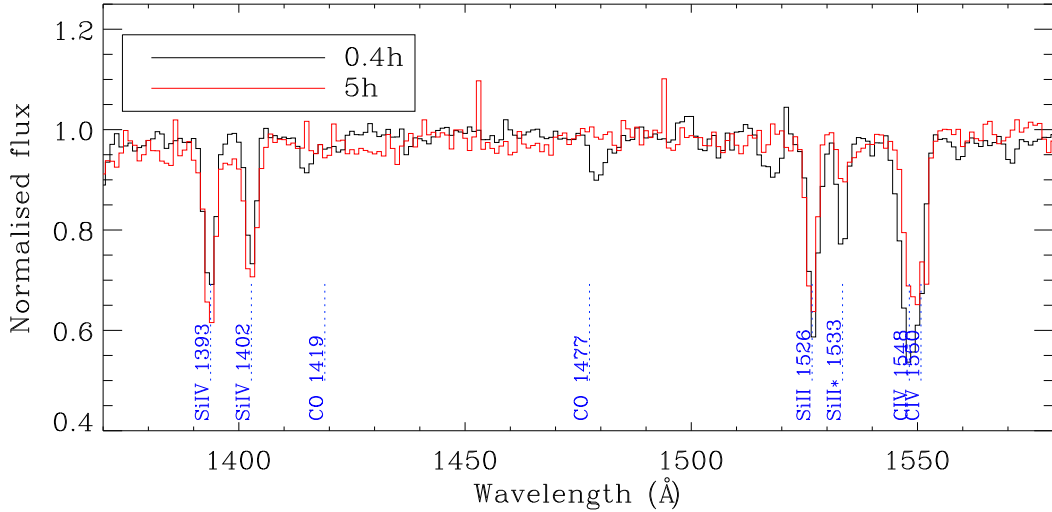


FIG. 3.— The composites show smaller variations within 20% for the high ionization lines CIV $\lambda\lambda$ 1548,1550 and SiIV $\lambda\lambda$ 1393,1402. Note the disappearing CO lines and weakening of the Si II* line.

A trend between the GRB isotropic energy release and the afterglow brightness has been found (Kann et al. 2010), albeit with a very large scatter possibly due to variations in the circumburst density. Because of this possible connection, we explore the effects for the composite spectrum by the GRB energy release. GRBs and their afterglows are thought to be collimated with a typical beaming angle between $1-25^\circ$ (Frail et al. 2001). Out of the 60 afterglows investigated here, 42 bursts have a measured bolometric isotropic energy (Kann et al. 2010, and references therein). These 42 bursts have energies between $51.38 < \log E_{\text{iso,bol}}(\text{erg}) < 54.49$.

We investigated the effects for the composite spectrum by dividing the sample into two samples according to the estimated bolometric, isotropic energy release from the prompt emission. Each subsample con-

tains 21 GRBs. The energy at which the sample is divided is determined by statistical sampling rather than a physically real property. The low and high energy composites have $51.38 < \log E_{\text{iso,bol}}(\text{erg}) < 52.88$ and $52.88 < \log E_{\text{iso,bol}}(\text{erg}) < 54.49$, respectively. Overall, there is no significant difference between the absorption line widths for either the high or low-ionization lines, and fine-structure lines are present in both the high-energy composite and low-energy composite. However, redward of 2200 Å, all lines (Fe, Mn, Mg) in the low-energy composite are a factor of ~ 4 weaker. The reason for this is most likely due to the fact that a couple of high-energy GRB afterglows at $z \sim 1$ (GRB 061121 and GRB 080413) have rather strong Fe absorption lines and dominate the absorption lines at rest-frame wavelengths larger than 2200 Å. Neglecting these two GRBs, the high- and low-

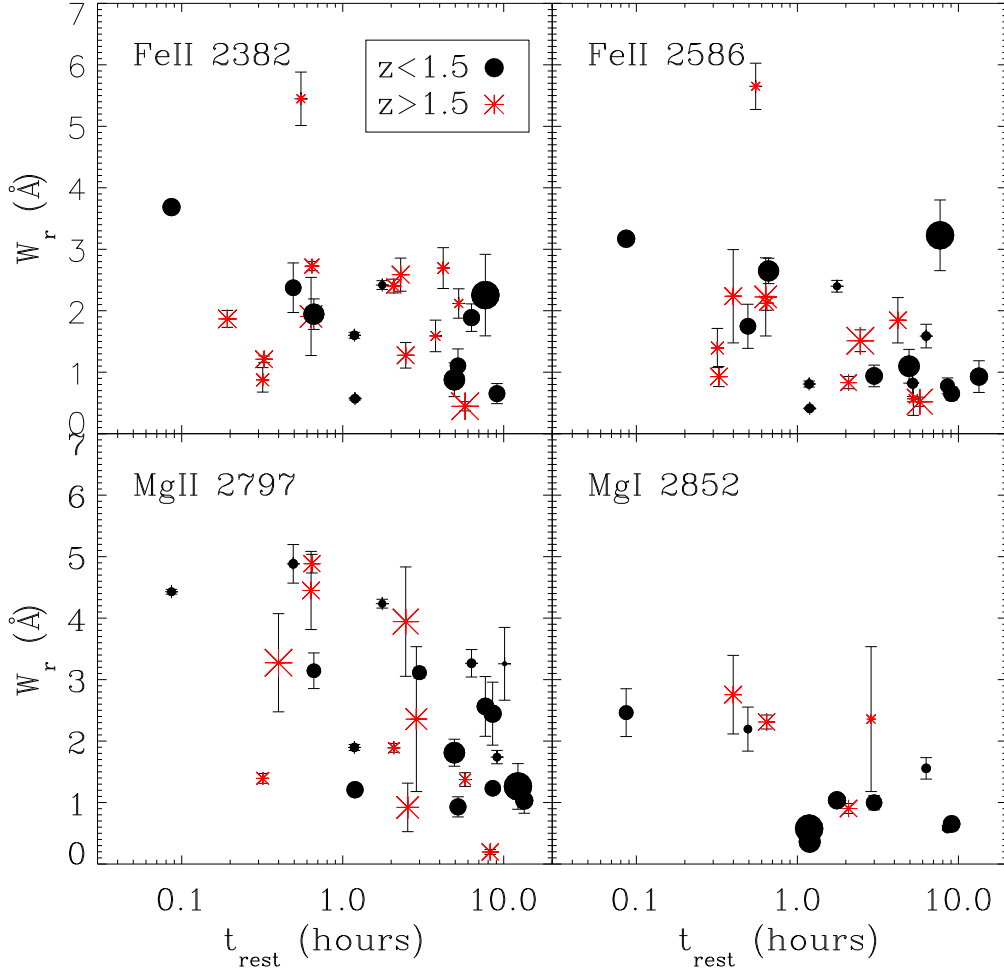


FIG. 4.— Rest-frame equivalent widths measured for individual bursts at $z < 1.5$ (dots) and $z > 1.5$ (crosses). The symbol sizes scale with the logarithm of the S/N of the individual spectra. Both early and late time GRBs have spectra with a good S/N.

energy composite spectra are similar, and the variations between the lines widths are $11\% \pm 22\%$ with no systematic trends of which of the low- or high-energy composites produce the strongest lines. We conclude that the prompt GRB energy release itself has no effect on the absorption lines.

4.6. Dark bursts

For some bursts, afterglows are not detected, but the success of detecting the afterglows depend strongly on the afterglow search strategies, i.e., rapid searches which are able to probe faint magnitudes. Some bursts may be dark, because they lie at high redshifts and are therefore not detected in optical follow-ups. Others may be obscured by dust. A better method to define intrinsically dark bursts relies on the X-ray flux versus the simultaneous optical afterglow magnitude. From this optical to X-ray spectral index, Jakobsson et al. (2004) define dark bursts as those having $\beta_{\text{OX}} < 0.5$.

In the sample of 60 afterglows, 53 have measured β_{OX} (Table 73 in F09), and 10 of these satisfy the criterion for being a dark burst. We created composite spectra for those with $\beta_{\text{OX}} < 0.5$ and $\beta_{\text{OX}} > 0.5$, but because of the large difference in the number of spectra that go into the composite, the S/N is also unequal. The composite spec-

trum from the bright burst sample with $\beta_{\text{OX}} > 0.5$ has an S/N between 100 and 200 from 1000 to 3000 Å, while the composite from the dark burst sample with $\beta_{\text{OX}} < 0.5$ has a S/N = 25–40 in the same wavelength region. Still, the dark burst composite has stronger absorption lines by a factor of 2–3 over this spectral range, while H I column density decreases by 0.2 dex from the bright to the dark composite. A representative wavelength region is shown in Fig. 5.

While the optical to spectral index separation at $\beta_{\text{OX}} = 0.5$ is based on a physical reasoning, we may still wonder if artifacts are included from comparing two spectra with very different S/N ratios. Choosing instead a different separation of β_{OX} for the subsamples may involve bursts with slopes that are dependent on the particular positions of the spectral breaks between the optical and X-ray bands. Although the separation is not arising from a physical explanation, the low- β_{OX} sample will still include the ‘darkest’ bursts. Dividing the full sample into two equal size parts instead with a separation in the spectral index of $\beta_{\text{OX}} = 0.75$ such that the S/N is comparable, consistently shows that the darker bursts have stronger absorption lines. The detection of stronger metal absorption lines towards dark bursts is fully con-

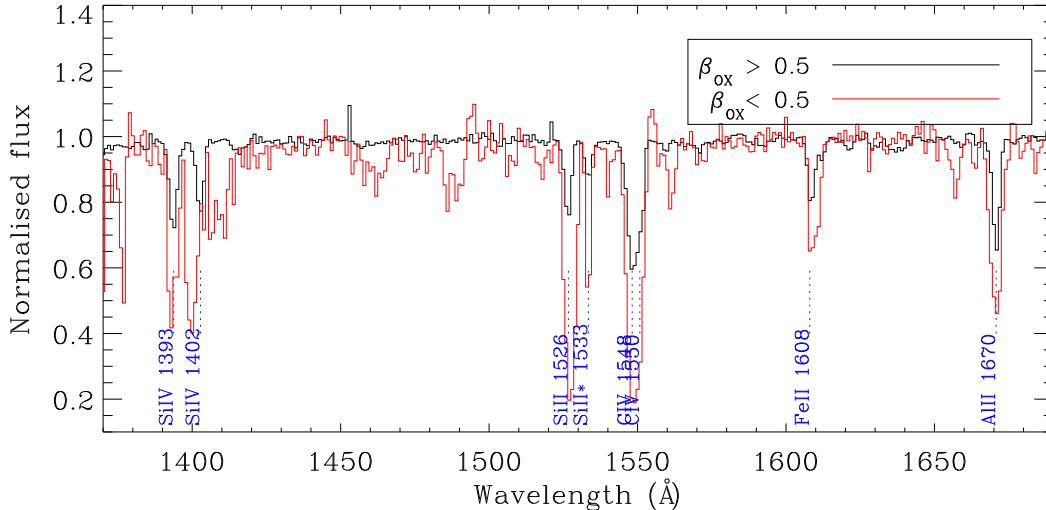


FIG. 5.— Dark bursts with optical to X-ray spectral slopes $\beta_{\text{OX}} < 0.5$ have stronger low ionization, high ionization and fine-structure absorption lines compared to the optically brighter ones with slopes $\beta_{\text{OX}} > 0.5$.

sistent with the idea that these reside in more metal-rich, dustier ISM relative to the bright counterparts. This is already established from analysis of the properties of the host galaxies from broad band photometry (Perley et al. 2009) and from X-ray absorption (F09).

4.7. Afterglow optical luminosities

The optical luminosities of the afterglows depend on a large number of parameters, including the density of the external medium. Although the medium which causes the absorption lines in afterglow spectra is generally determined to lie at distances greater than 1 pc, we may still investigate if the composite spectrum shows any changes related to the optical luminosities. Potentially, some absorption lines may arise closer to the GRB explosion than otherwise determined, or there may be an anti-correlation between a more dusty, metal rich environments and the optical luminosity of the afterglows.

Having investigated the effect of the spectral slopes, we include an analysis of any systematic effects of the afterglow optical brightness. Analyzing the light curves in a systematic way, Kann et al. (2010) determine the observable, extinction corrected magnitudes of a large number of afterglows at $t = 1$ day from the explosion in the rest frame of the bursts. The R_C magnitudes are listed for 39 of the 60 bursts in the composite sample. We divide the spectra into two almost equal sized subsamples separated at $R_C = 19.55$ mag. The two resulting composites have the same S/N ratio.

The optically faint subsample has stronger Fe II lines redward of 2200 Å compared to the bright subsample. While the high ionization lines in the two samples are of the same strength, the low-ionization ones are about 50% stronger in the faint sample. As for the isotropic energy release case, two bursts (GRB 061121 and GRB 080413) are among the optically faint ones 1 day after the explosion. At the time when the spectra were obtained they were among the brighter ones. Eliminating these two GRB afterglows from the faint sample, the composite spectra have similar absorption line strengths.

5. METAL ABSORPTION LINES

In this section, we compare the individual features in the composite spectrum with other categories of absorption line systems with the purpose of investigating whether GRB environments are special. This is interesting in the context of constraining the nature of the GRB progenitor through any peculiarities in the surrounding medium.

5.1. Strong Ca II and Mg II absorbers

The composite spectrum displays a large number of absorption lines. To compare the composite with other high redshift galaxy spectra, we are limited to the stronger transitions found in large samples in low spectral resolution data, because these are the ones most easily detected in faint galaxy spectra.

The Ca II absorption lines are very strong in the composite with $W_r^{\text{Ca II } \lambda 3934} = 0.77$ Å, which places the average GRB site in the category of the dustiest absorbers (Zych et al. 2009) compared to other intervening absorptions systems selected by their neutral hydrogen column densities. In intervening quasar absorbers at lower redshifts, strong Ca II lines belong to DLAs with a color excess of $E_{B-V} > 0.1$ mag (Wild et al. 2006). The reverse is not true; only 10% of DLAs have strong Ca II lines (Nestor et al. 2008), and DLA selected absorbers have an order of magnitude less reddening ($E_{B-V} < 0.02$ mag in Murphy & Liske 2004).

Also the Mg II absorption lines fall among strong, but not extreme absorbers detected in quasar spectra (Nestor et al. 2005). Its $W_r^{\lambda 2797} = 1.7$ Å is common for systems associated with DLAs (Rao et al. 2006). The Mg II W_r is smaller than the $W_r = 3.8$ Å found in a composite spectrum of local starburst galaxies (C. Tremonti, private communication) as well as ultra strong ($W_r > 3.0$ Å) Mg II absorbers at $z = 0.7$ (Nestor et al. 2010), which possibly trace starburst galaxies (Rubin et al. 2010). The widths of Mg II lines in quasar spectra which arise in intervening galaxies at $0.3 < z < 1$ also depend on the galaxy's rotation and inclination (Kacprzak et al. 2010).

Since GRB hosts have low stellar masses (Savaglio et al. 2009), star burst driven galactic winds would easily escape their potential well. Strong lines with large W_r such as Si II $\lambda 1526$ have very large optical depths such that the line widths measure the velocity spread of individual components in DLA systems both towards quasars and GRBs (Prochaska et al. 2008a). Large widths can therefore be seen as proxies of galaxy wind strengths, which would indicate that GRB hosts have weaker winds relative to galaxies with higher absolute star formation rates (SFRs). Higher resolution spectra are needed to explore the effects of galaxy winds in GRB hosts in order to quantify the effect the host mass and SFRs on the absorption line widths of the very strong lines.

5.2. Dusty afterglow spectra

There is currently little evidence either for a strong extinction from the afterglows themselves with typical values of $E_{B-V} < 0.3$ (Galama & Wijers 2001; Kann et al. 2006), while a few individual bursts suffer from more extinction like GRB 070306 which had $A_V = 5.5 \pm 0.6$ mag (Jaunsen et al. 2008) and GRB 070802 which had $A_V = 0.8 - 1.5$ mag and showed a pronounced 2175 Å bump (Elíasdóttir et al. 2009). These two GRB spectra have relatively low S/N, so they do not affect the composite significantly. Recently, a very high extinction of $A_V > 12$ was suggested for the dark burst GRB 090417B (Holland et al. 2010). However, such dusty environments are rare in the sample studied here, where the extinction measured from the afterglows is generally low (Kann et al. 2010).

In the integrated spectral energy distribution (SED) of the host galaxies there is evidence for relatively little reddening around $E_{B-V} \sim 0.1$ (Christensen et al. 2004; Savaglio et al. 2009; Levesque et al. 2010), although fits to SEDs which include the far-IR emission find larger amounts of extinction in GRB hosts (Michałowski et al. 2008). Analyses of individual afterglow spectral slopes generally only allow for small amounts of extinction in the burst region (Kann et al. 2010). If no dust is present in the host galaxy, this would produce a brighter optical afterglow and introduce an observational bias (Fynbo et al. 2001). For some GRBs no optical afterglow is detected (Jakobsson et al. 2004), which is most likely due to dust obscuration in their host galaxies (Perley et al. 2009, ; F09). However, for the composite spectrum of bursts with detected optical afterglows, dust obscuration is not a strong effect.

5.3. Molecular lines and diffuse interstellar bands

We search the composite for absorption lines arising from molecular lines, but only CO lines are found. These are very rare in GRB sight lines, and the composite is dominated by the strong CO lines observed in GRB 080607 and which are caused by excitation from the GRB (Prochaska et al. 2009; Sheffer et al. 2009). A possible, but weaker detection is that towards GRB 060210 (F09). Eliminating the GRB 080607 afterglow while creating the composite, the two detected CO lines in the composite vanish (see Fig. 3). Regarding other molecular lines, H₂ absorption lines are not commonly found in GRB afterglows (Tumlinson et al. 2007; Ledoux et al. 2009). The strong H₂ lines observed in the line of sight

to GRB 080607 are blended with too many other lines in the composite Ly α forest, so we cannot include a more detailed study here.

We also search for diffuse interstellar bands (DIBs) redward of 4000 Å using a list of DIBs found in the Galaxy (Jenniskens & Desert 1994). In particular, we look for the strongest bands at $\lambda 4428$, $\lambda 5705$, $\lambda 5780$, $\lambda 5797$, $\lambda 6010$, $\lambda 6203$, and $\lambda 6283$, which apart from seen in Galactic sight lines, are also found in nearby starburst galaxy spectra. Some of these lines have recently been observed in a high-resolution spectrum of the Type Ib SN 2008D which exploded in NGC 2770 (Thöne et al. 2009), showing that DIBs can be present in galaxies which form massive stars. These lines are found to have typical strength of > 0.1 Å, and their equivalent widths correlate with the color excess E_{B-V} and the hydrogen column density (Heckman & Lehnert 2000; Welty et al. 2006). Even considering the very high $N(\text{H I})$ in the composite, we failed to get any significant detection although the spectral range and S/N ratio for the composite is sufficient to find some of the bands with $W_r \approx 0.1$ Å. Welty et al. (2006) derive a best-fit relation between the 5780 Å DIB strength and the reddening in Galactic sight lines. Using their fit $\log E_{B-V} \approx -2.7 + 1.1 \log W_r(5780)/\text{mÅ}$, the limit for W_r corresponds to an upper limit of $E_{B-V} < 0.3$ mag. A similar reddening limit would be inferred by a UV-shielded line of sight in the Small Magellanic Cloud (Cox et al. 2007).

Relative to stars in the Galaxy, weaker DIBs are found in the less metal-rich medium of the Magellanic Clouds (Welty et al. 2006). A higher ionizing radiation field than that present in the Galaxy may be responsible for destroying the carriers of the molecules that give rise to the DIBs (Welty et al. 2006; Cox et al. 2007). Apart from detections of DIBs in the Galaxy, DIBs have been found in some gas-rich galaxies. Lawton et al. (2008) find that strong DIBs are absent in six out of seven DLAs at $z < 0.5$, with the one detection belonging to the most metal rich system with the highest reddening (Junkkarinen et al. 2004). Like the DLA systems, the average GRB host ISM is also metal-poor and contain relatively little dust. Additionally, GRB regions are known to have strong radiation fields (Levesque et al. 2010), and therefore the DIB carriers are likely to be destroyed in the region near the GRBs. These arguments combined may be the reason for the non-detection of DIBs in the composite spectrum.

The most commonly found DIBs fall in the rest frame visible region of the composite spectrum which has a significantly smaller S/N ratio, and where only few afterglows contribute. It would be more useful to look for DIBs in the UV part of the spectrum, which allows the detection of weaker lines. Some unidentified UV features with equivalent widths of a few to a few tens of mÅ possibly belonging to diffuse bands have been identified in spectra of Milky Way stars (Pwa & Pottasch 1986; Destree & Snow 2009). Of the few UV DIB candidates suggested, most lines lie too close to other metal absorption lines in the low-resolution composite spectrum to allow their identifications. Two exceptions are UV features at 1384.3 Å and 1490.1 Å, which are not detected in the composite afterglow spectrum to a 3σ limit of 60 mÅ. The features observed in stellar spectra are even weaker

than this detection limit, so if UV DIBs are present in GRB spectra an even better S/N ratio is necessary to be able to detect them.

5.4. High-ionization Lines

In almost all low redshift starburst galaxies, the Si IV $\lambda 1400$ and C IV $\lambda 1550$ lines are quite strong with rest-frame equivalent widths $> 3 \text{ \AA}$ as seen in HST spectra of local starburst galaxies (C. Tremonti, private communication). In the afterglow composite, the absorption lines are weaker with $W_r = 1$ and 2 \AA , respectively. The transitions arise as a combination of stellar wind features and intrinsic ISM absorption. In starburst galaxies, the wind component is typically recognized from their P-Cygni profiles. Contrary to direct spectra of starbursts, the GRB afterglow spectra are not the direct emission associated with massive stars, so with the absence of a recognizable P-Cygni profile in the GRB afterglow spectra, a lower W_r is expected.

The C IV and Si IV lines typically extend over several hundreds of km in GRB spectra, and have several components some of which are saturated (Prochaska et al. 2008a; Fox et al. 2008, ; F09). In the low-resolution composite spectrum these lines have residual relative fluxes < 0.7 , which suggests that they are composed of individual saturated lines as explained in Sect. 7.

The highly ionized gas could potentially trace the medium surrounding the GRB progenitors. Species like N V and O VI require a stronger ionizing radiation field than that produced by O stars, but which can be produced by a GRB event (Prochaska et al. 2008b), although the creation by collisional ionization in the ISM cannot be ruled out (Fox et al. 2008). The N V $\lambda \lambda 1238, 1242$ doublet is distinguishable in some of the individual afterglow spectra at low resolution, while in high resolution spectra reveal that these lines are ubiquitous (Prochaska et al. 2008b; Fox et al. 2008). These lines are not easily recognizable in the composite spectrum, because they are blended with the red wing of the Ly α line, in particular in spectra with high signals and very high H I column densities. In the composite spectrum the N V lines appear as a slight deviation from the broad wing profile of Ly α . A more detailed analysis of these line requires a higher spectral resolution.

6. COMPARISON WITH STARBURST GALAXY SPECTRA

With a high S/N composite it is relevant to look for differences in the absorption line properties compared to what is known about other galaxies. With a spectral range covering from the UV to the rest-frame optical wavelengths, a comparison with local starburst galaxies is justified, but given the redshift difference it is more appropriate to compare with starburst galaxies at higher redshifts. Such a comparison is hampered by the faintness of the distant galaxies, but in a few cases a good signal from high redshift galaxies have been obtained.

A low resolution composite spectrum from 811 Lyman break galaxies (LBGs), which has a measured S/N of ~ 40 and a rest-frame wavelength coverage from 920 to 2000 \AA is presented in Shapley et al. (2003). The composite LBG spectrum has been created by averaging the spectra of galaxies at $z > 3$ with magnitudes $R \lesssim 25.5$, and the composite spectrum has a dispersion of 1 \AA pixel^{-1} . With an average redshift $z \sim 3$, this is

comparable to the GRB composite spectrum. Another example is the magnified signal from high redshift galaxies lensed by foreground galaxies or clusters. The prototype LBG spectrum obtained with Keck/ESI of MS 1512-cB58 (cB58 for short) at $z = 2.7276$ (Pettini et al. 2000, 2002), which covers 1050–2800 \AA in the rest-frame and has an S/N ~ 2 –15, presents another valid comparison for the GRB composite. Finally, we also compare the GRB composite with a UV composite spectrum of UV bright galaxies at $1.3 < z < 2$ from the Gemini Deep Deep survey (GDDS) (Savaglio et al. 2004), which covers the wavelength range 2000–3000 \AA with an S/N of about 15.

Fine-structure lines can arise in a medium which is being pumped by UV radiation, or in very high density regions (Silva & Viegas 2002). Fe II* fine-structure lines have been detected in several GRB sight lines but not in quasar absorption systems (Chen et al. 2005), and locally only in the dense wind from η Carinae (Gull et al. 2005). The UV pumping scenario and the time variations of the absorption lines in time series observations of individual bursts indicate a decrease of the ionizing radiation from the GRB (Prochaska et al. 2006). In this scenario, one would only expect the presence of Fe II* fine-structure lines to be related to the environment in the GRB host galaxy, and generally not to be present in the ISM in normal starburst galaxies.

Since long duration GRBs explode in star forming galaxies (Christensen et al. 2004), we here investigate if the fine-structure lines could be present generally in starburst galaxies which have particularly large SFRs, or strong emission in the UV, or emission arising from dense environments. In a composite spectrum created from local starburst galaxies (C. Tremonti private communication) most of the metal absorption lines in the range 2150–3250 \AA identified in the GRB composite are also present (See Figure 6). The strongest transition is that from Fe II* $\lambda 2396$ which is clearly detected in the GRB composite, but due to the lower quality of the starburst composite (S/N ~ 30), we cannot claim a clear presence of Fe II* fine structure lines. A better signal from a starburst galaxy is needed to establish if these lines are only present in the most extreme conditions in the region around a GRB explosion either by being pumped by the hard UV radiation, or by having a specially high density.

In terms of tracing starburst galaxies, LBGs are brighter and more massive than GRB hosts at the same redshifts due to the selection of bright sources for the LBG samples, whereas GRBs trace star forming galaxies irrespectively of their brightness. The same selection effects play a role for the galaxies in the GDDS, while cB58 has an intrinsic brightness of a typical L^* galaxy. None of the comparison spectra show Fe II* lines; in the case of cB58 the lines around 1600, 2300, and 2600 \AA could have been detected if they had been there. The non-detection of fine-structure lines in starburst galaxies is perhaps not surprising given that Fe II* lines in afterglow spectra decay rapidly after the burst, and on that basis the lines are not expected to be present on the much longer timescales present for regions where massive stars are formed.

With a few exceptions, the W_r measured for cB58 in Pettini et al. (2002) have typical values about twice the strengths of those in the GRB composite. The exceptions

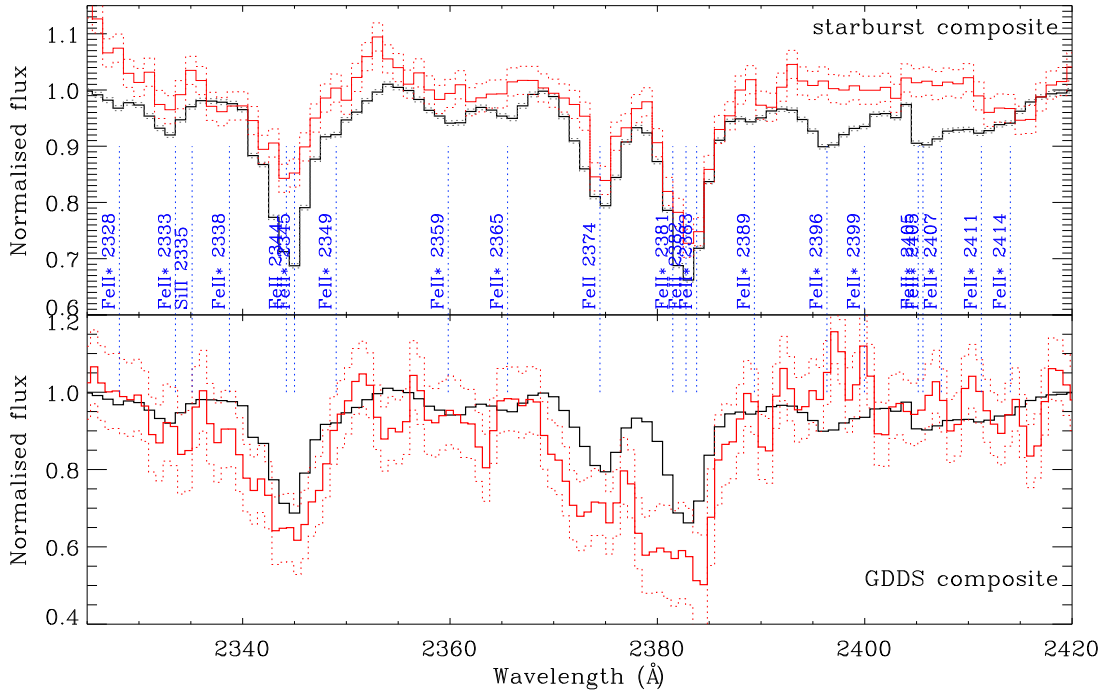


FIG. 6.— Section of the GRB afterglow composite spectrum (in black) compared to a starburst galaxy composite spectrum in red in the *upper panel* (from C. Tremonti). The dotted lines correspond to 1σ deviations from the composite. While strong Fe II^* fine-structure transitions are present in the GRB composite, only the those from the ground state are present in the starburst composite. The *lower panel* shows the same region for the GDDS composite spectrum.

are the $\text{Fe II } \lambda\lambda 1608, 1611$ blend, Cr II , $\text{Zn II } \lambda 2026$ and Cr II , $\text{Zn II } \lambda 2062$ blends, and the $\text{Mn II } \lambda 2577$ line, all of which have roughly the same line strengths as in the GRB composite. In contrast, the LBG and GDDS spectra have in general line strengths in between the GRB composite and cB58 (see also Table 2 in Savaglio et al. 2004).

LBGs and GDDS galaxies are relatively more massive, have higher SFRs, and have stronger outflows driven by massive stars and supernovae relative to the GRB hosts. The SFRs derived from the UV continuum flux relative to the GRB hosts luminosities are comparatively high (Christensen et al. 2004). In contrast the specific SFR (SFR per unit stellar mass) is found to be low compared to other high redshift galaxies (Castro Cerón et al. 2006, 2010), while Savaglio et al. (2009) find the contrary. It is therefore still an open issue as to which degree the line strengths in GRB hosts and other high redshift galaxies are related to their specific SFRs.

The $\text{C IV } \lambda\lambda 1548, 1550$ lines are stronger in all comparison spectra. This line arises as a combination of ISM and stellar, outflow driven, absorption components. Since the GRB hosts are generally very faint, the emission from the host does not dominate, such that no P-Cygni profiles are expected in the GRB afterglow spectra. Other exceptions are the Si II^* lines which are found in absorption in the afterglow composite, while these lines are found in emission in the cB58 spectrum and the LBG composite.

7. COLUMN DENSITIES

The hydrogen column density for cB58 is about one order of magnitude below that in the GRB composite: $\log N(\text{H I}) = 20.85$ resulting in a higher metallicity of 40% solar (Pettini et al. 2002). Since the widths of the metal absorption lines in the GRB spectrum are generally lower than in other high redshift galaxies, one is led

to the question of what is the average metallicity in GRB lines of sight. However, this is a complex issue to address using the GRB composite spectrum, because each absorption line does not measure the same samples of individual GRB lines of sight. Any composite spectrum will carry along the scatter of properties of the individual objects (galaxies or GRB afterglows) that went into it in the first place, and a physical interpretation is hampered by this. Still, the general features in a composite spectrum can be derived, as done from the LBG composite with its interstellar absorption lines (Shapley et al. 2003) and for the GDDS composite, where the trends of metal column densities, depletion patterns and extinction were derived for galaxies at $1.4 < z < 2$ (Savaglio et al. 2004). Compared to these studies, the GRB afterglow composite may present further complications, because the galaxies probed by the random sight line of a GRB through their ISMs are not as uniformly selected.

Bearing this in mind we analyse the metal lines to derive column densities for a wide range of elements. Since the spectra are obtained at low spectral resolution, we use a standard single component curve-of-growth (COG) method to calculate the column densities. For GRB spectra which have absorption lines with multiple, saturated components spread over a velocity range of several 100 km s^{-1} , the simple COG method underestimates the true metal column densities and the metallicities can be larger by up to 1 dex in the worst case scenario (Prochaska 2006).

In the case of H I, its column density is determined instead from Voigt profile fitting to the red wing of the absorption line. In the COG fit, the best fit Doppler parameter (b) is determined using ten individual Fe II lines. Including all the uncertainties of the lines, a best fit yields

$b = 44 \pm 2 \text{ km s}^{-1}$ and $\log N(\text{Fe II}) = 15.62 \pm 0.05$. However, as demonstrated in Prochaska (2006), the weaker lines in the linear part of the COG have underpredicted strengths, and the true column density may be larger than given by the best fit. Instead, we choose to tie the fit to the four weaker lines (Fe II $\lambda 1611$, $\lambda 1901$, $\lambda 2249$, and $\lambda 2260$) as illustrated in Fig. 7. Since the widths of the stronger iron lines have been calculated by deblending them from the Fe II* fine-structure lines, some contamination may still occur, in particular for the Fe II $\lambda 2382$ and Fe II $\lambda 2600$ lines. The best fit is determined from χ^2 minimization, which gives a Doppler parameter $b = 34 \pm 2 \text{ km s}^{-1}$ and $\log N(\text{Fe II}) = 15.70 \pm 0.07$. All Fe II lines follow a single curve well both in the linear part, while the points in the flat part show some scatter around the best fit COG. To assess the amount of contamination by the fine-structure lines, we examine the composite spectrum created from the late-time sample in Sect. 4.4. We measure the W_r for the 10 Fe II lines and find the best fit with a smaller Doppler parameter: $b = 20 \pm 2 \text{ km s}^{-1}$ and $\log N(\text{Fe II}) = 15.60 \pm 0.10$.

Since low resolution data indicate a higher b parameter than when observed at high resolution, because it measures the spread of the lines (Prochaska 2006) rather than the intrinsic velocity of the gas, it is relevant to compare with individual measurements of b from detailed high resolution spectra. Typical Doppler parameters measured in various GRB afterglow spectra are between 7 and 15 km s^{-1} (Fiore et al. 2005; Chen et al. 2007; Thöne et al. 2007; D’Elia et al. 2009a,b), while Vreeswijk et al. (2007) found $b = 25 \text{ km s}^{-1}$ for GRB 060418. Hence, the reason for our finding of a higher b is partly due to blending with iron finestructure lines, while a minor remaining part could be caused by intrinsic line spreads of different components in a line.

To derive column densities for other elements, we use the best-fit b parameter from the fit to the iron lines. Column densities for all the elements are listed in Table 5. We avoid using lines which are obviously blended with other elements as for example the O I $\lambda 1302$ and Si II $\lambda 1304$ blend. To derive the column density of Zn II, we subtract the contribution of the Cr II $\lambda 2062$ to the total width of the line. From fit of the other two Cr II lines to the COG we find that $W_r^{\text{Cr II } \lambda 2062} = 0.17 \text{ \AA}$, whereas the Cr II $\lambda 2026$ line makes an insignificant contribution to the Zn II $\lambda 2026$ line. If the column density of Mg I is low as the best fit suggests in Sect 7, then the contribution of Mg I $\lambda 2026$ to the line blend is 0.05 \AA , which we subtract for the fit to the Zn II column density.

We checked whether the composite spectrum is reliable for the analysis of the metal column densities by comparing the fits with the spectrum derived from Eq. (3). Using the ten Fe II lines, we get a consistent result with the best fit of $\log N(\text{Fe II}) = 15.90 \pm 0.10$ and $b = 30 \pm 2 \text{ km s}^{-1}$. With a lower S/N, this composite does not allow us to derive column densities of all the weak lines and rare elements.

The elements are shown in Fig. 7 as different symbol shapes. This plot illustrates that in general, the absorption lines fit well to the Fe II COG apart from at low values of $\log(Nf\lambda \text{ (cm}^{-1})) \lesssim 7$, where the scatter may have a physical explanation. To mention a few elements in particular, the Ti II lines are relatively weak,

and the scatter for the six detected lines for this element in Fig. 7 is substantial. Also some of the Mg I lines are out-lying relative to the COG. The main reason is possibly the sampling of the absorption lines by different GRBs. Since the Mg I lines lie in the range 1747–2852 Å and Ti II lines in the range 1906–3384 Å, each absorption line must sample a different set of GRBs. In these cases, we exclude points with $\log(Nf\lambda) \lesssim 7$, but warn that in reality the column densities for these elements could be ~ 1 dex *higher* than listed in Table 5. The same tendency is observed for Fe I lines. At the other end of the scale, Si II $\lambda 1260$ and Si II $\lambda 1808$ are blended with their respective fine-structure lines, and are not possible to deblend. As a consequence, the Si II lines in Fig. 7 scatter and we base the fit for the column density mostly on the isolated Si II $\lambda 1526$ line. Since the only singly ionized carbon line (C II $\lambda 1534$) detected in the composite is blended with C II* $\lambda 1335$, we cannot calculate its column density accurately. Instead, we assume that the two lines contribute roughly equally to the total line strength such as observed in GRB 050730 (Prochaska et al. 2007a).

The majority of the singly ionized species listed in Table 5 have ionization potentials above 13.6 eV, and with the high column densities these are generally the dominant species in DLAs. The metallicity of the different elements are given relative to the solar value $[X/H] = \log(N_X/N_H) - \log(N_X/N_H)_\odot$ in column 5 in Table 5. Where column densities from different ionization levels are derived, the metallicity corresponds to their sum. Different elements show relative metallicities in the range of 1%–10% solar. In high column density media, the dominant state of Ca is Ca III, so the low relative metallicity of Ca II does not reflect the real metallicity of this element. Also the Mg II lines are saturated, so the metallicity is a lower limit.

To check the derived column densities for consistency, we also use the apparent optical depth (AOD) method (Savage & Sembach 1991), which is valid for non-saturated lines. In low resolution data, intrinsically saturated lines are smoothed and do not appear saturated. In practice we find that lines with residual flux $\lesssim 0.7$ in the composite spectrum are most likely to be saturated, and using these lines will only give a lower limit for the column densities. Column 6 in Table 5 lists the column densities of the various species, where the individual lines were integrated from -600 km s^{-1} to $+600 \text{ km s}^{-1}$. We avoided as best possible the individual saturated lines as well as lines which are blended with other species. Comparing columns 2 and 6, the agreement between column densities derived from the COG and the AOD methods is good. The exceptions are Fe I and Mg I, where the AOD method depends strongly on what lines are used to derive the column densities. For example the Mg I $\lambda 2852$ suggests a much lower column density $\log N = 13.06 \pm 0.10$ compared to that derived from the other two lines (Mg I $\lambda 1748$ and Mg I $\lambda 1828$ which indicate $\log N = 14.20 \pm 0.10$). The large difference in column density can be due to the fact that the Mg II $\lambda 2852$ line is saturated. Further, these lines also exhibit a large scatter in the COG plot, and may as explained above be the result of a physical difference in the medium probed by the GRBs.

8. DISCUSSION AND FUTURE PROSPECTS

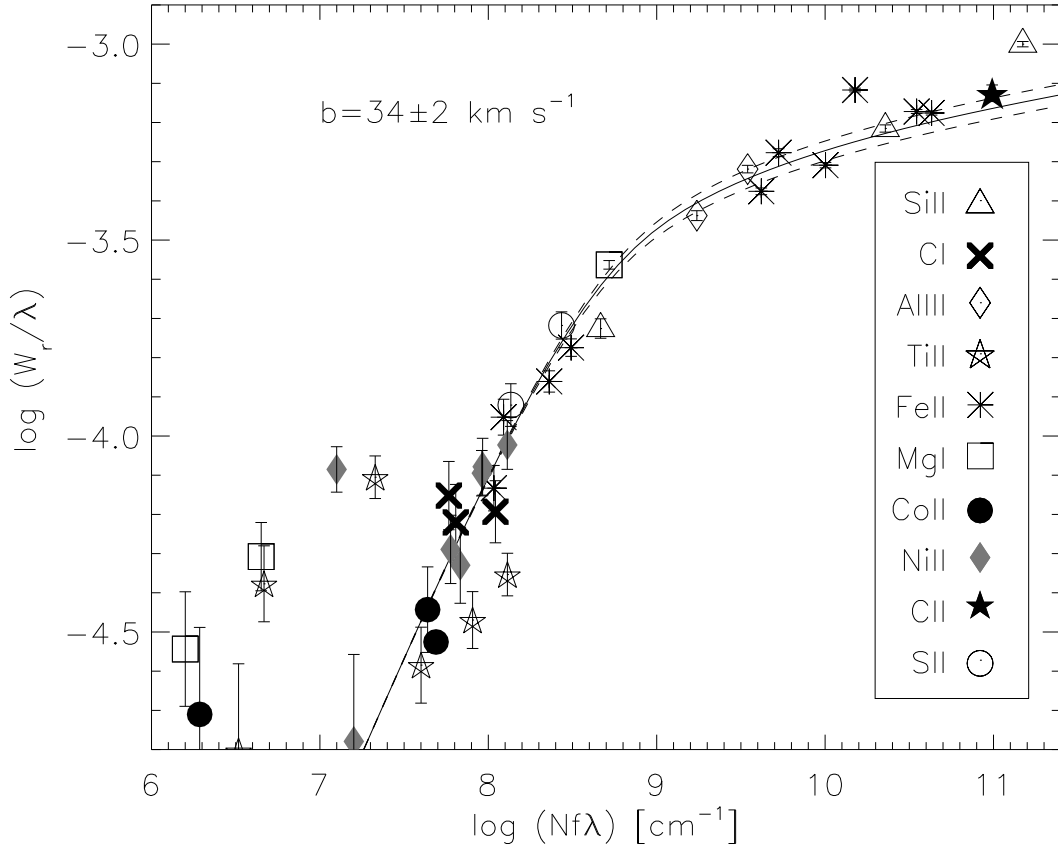


FIG. 7.— Curve-of-growth with the best Doppler parameter (and $\pm 1\sigma$ uncertainties) fit estimated from ten Fe II lines. Other elements, are overplotted and all best fit column densities are listed in Table 5.

Having analyzed a series of parameters, which may affect the strengths of the metal absorption lines in GRB afterglows we arrive at the following results.

- Variations in excited states are apparent.
- No variations in the ground states.
- No correlation with GRB energy release.
- No correlation with optical afterglow brightness one day after the GRB.
- Dark bursts have stronger lines.

These results suggest that the medium surrounding the GRB at a significant distance is mainly responsible for the strengths of the absorption lines, and that the GRB itself plays a minor role. Only the excitation of the fine-structure lines by the immediate ionizing radiation appear to reflect the impact of the GRB explosion. That some afterglows are bright and have either strong or weak absorption lines, may just reflect the diverse nature of the ISM along different lines of sight through high redshift galaxies.

Characterizing the physical parameters from the composite is difficult because each absorption line has a different sample of individual GRB spectra contributing to it. As such the composite is not relevant for determining the physical conditions present around a single GRB because it is a global average of different lines of sight

at a range of redshifts, where diverse conditions such as metallicities, abundance ratios, and densities may prevail. The results are therefore not directly applicable to a particular GRB environment. Biases may also hamper the comparison to individual GRB afterglows observed in the future, since the individual spectra which dominate the composite spectrum are relatively bright, and are not affected severely by dust obscuration.

These effects will inevitably influence the column densities of species, where their individual absorption lines lie far apart in wavelength. Although we estimate metallicities from several elements to be 1%–10% solar, we do not attempt to analyze the abundance patterns in comparison to the solar or depletion onto dust grains, because of the inherent uncertainty of the GRB sample. Interestingly, previous studies of individual GRB afterglows observed with low resolution spectroscopy have indicated ISM metallicities from 10%–100% solar (Savaglio 2006; Fynbo et al. 2006; Vreeswijk et al. 2006; Berger et al. 2006; Prochaska et al. 2007b; D’Elia et al. 2007), although a very low metallicity is reported for GRB 090926 (Rau et al. 2010). Conversely, afterglows observed at high spectral resolution show relatively lower metallicities (average 2% solar in Ledoux et al. 2009). The composite low resolution spectrum presented here is in better agreement with the high-resolution results and the more metal poor systems observed at low resolution. For multi-phased absorption systems the column densities and metallicities can be underestimated using a

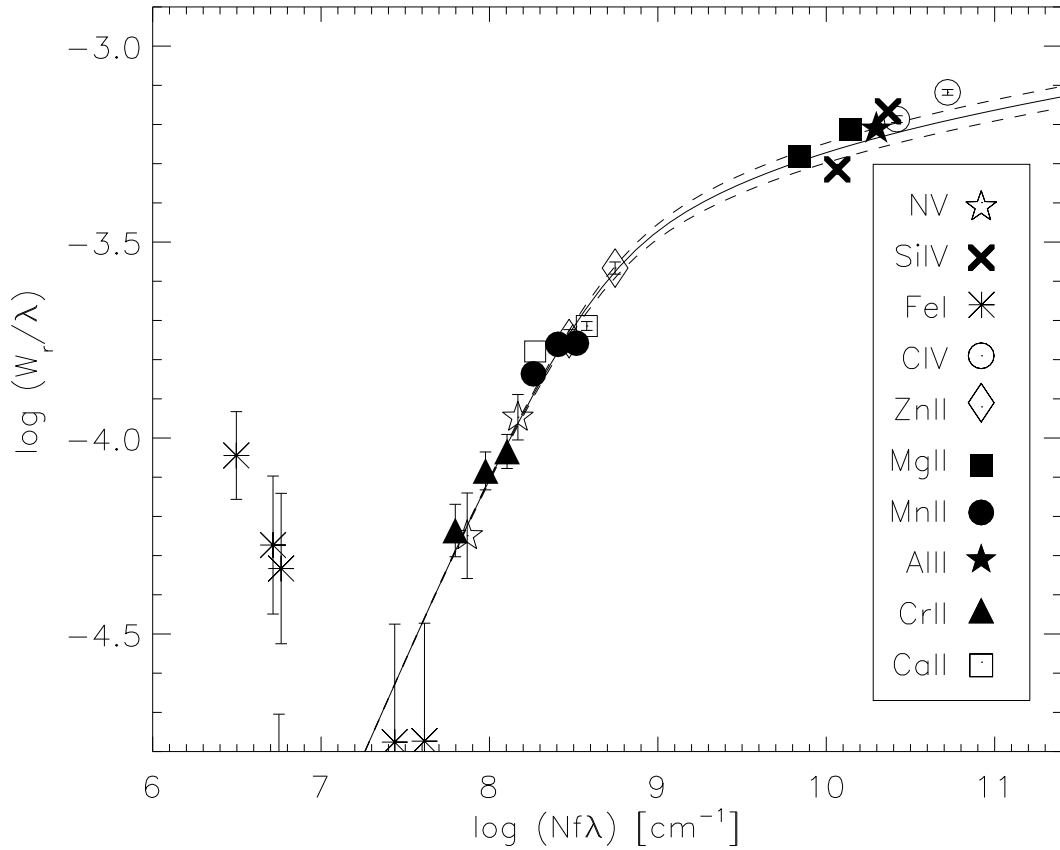


FIG. 7.— *continued.* Other elements are fit to the FeII COG.

COG analysis of low spectral resolution data (Prochaska 2006), which would then cause an even stronger discrepancy between the high- and low-resolution samples.

Although the composite spectrum cannot be used as an absolute reference scale to measure the relative strengths of a set of absorption lines, it can be used to discriminate special bursts which truly have outlying properties such as the pure high-ionization lines in GRB 090426 (Levesque et al. 2010; Thöne et al. 2010). With the recent advent of the wide wavelength coverage (3000–25000 Å), second generation VLT spectrograph, X-shooter (D’Odorico et al. 2006), this composite spectrum can serve as a reference for line identifications (see e.g., de Ugarte Postigo et al. 2010) in future GRB afterglow studies. A similar composite spectrum made from higher spectral resolution data would help to disentangle any of the temporal variations in the strong blends of lines from fine-structure and non-excited transitions.

The composite spectrum can also be used to derive the redshifts of very noisy spectra using a cross-correlation technique. We attempted this for GRB 060614 which did not show any detectable absorption lines in its spectrum (F09), but fail to determine a reliable redshift probably because of the absence of absorption lines rather than a bad S/N ratio. On the other hand, we determine tentative redshifts for GRB 070129 ($z = 2.985$), GRB 070508 ($z = 2.790$), and GRB 080523 ($z = 2.050$) consistent with possible, albeit noisy detections of either Si IV, C IV

or Al III lines in their spectra, and also consistent with the upper redshift limits in F09.

An important future study is to investigate the effect of the location of the GRB with respect to the host galaxy. The locations of high redshift GRBs follow the light distributions, and are typically found close to the brightest part of their host galaxy (Bloom et al. 2002; Fruchter et al. 2006; Svensson et al. 2010). We do not have the information of the spatial offsets available to make a comparison here. Logically, one could expect stronger absorption lines arising from GRBs which are located at smaller impact parameters to their hosts, but this hypothesis has to be verified first. Another line of investigation would be the correlation of absorption line strength versus the host galaxy brightness. Again we do not have sufficient data available to make this investigation. As discussed in Sect. 6, LBG galaxies show generally stronger lines, but are also selected among the intrinsically brighter high redshift galaxies which presumably are more massive and metal-rich than the average GRB host. Combined with the brightness, it would also be an interesting extension to investigate the correlations of absorption line strengths with the SFRs and specific SFRs of the GRB hosts.

We thank the anonymous referee for the constructive comments. The Dark Cosmology Centre is funded by the Danish National Research Foundation. We thank Hsiao-

Wen Chen, Sandra Savaglio, Palle Møller, Max Pettini, Sergio Campana, Daniele Malesani and Cedric Ledoux for helpful discussions. We also thank Christy Tremonti for supplying the starburst galaxy composite spectrum,

Sandra Savaglio for the GDDS composite, Chuck Steidel for the cB58 spectrum, and Josh Bloom and Hsiao-Wen Chen for sharing the reduced LRIS and GMOS spectra, and finally Paul Vreeswijk for sharing the FORS data.

REFERENCES

- Asplund, M., Grevesse, N., Sauval, A. J., & Scott, P. 2009, *ARA&A*, 47, 481
- Berger, E., Penprase, B. E., Cenko, S. B., Kulkarni, S. R., Fox, D. B., Steidel, C. C., & Reddy, N. A. 2006, *ApJ*, 642, 979
- Bloom, J. S., Kulkarni, S. R., & Djorgovski, S. G. 2002, *AJ*, 123, 1111
- Castro Cerón, J. M., Michałowski, M. J., Hjorth, J., Malesani, D., Gorosabel, J., Watson, D., Fynbo, J. P. U., & Morales Calderón, M. 2010, *ApJ*, 721, 1919
- Castro Cerón, J. M., Michałowski, M. J., Hjorth, J., Watson, D., Fynbo, J. P. U., & Gorosabel, J. 2006, *ApJ*, 653, L85
- Chen, H.-W., et al. 2009, *ApJ*, 691, 152
- Chen, H.-W., Prochaska, J. X., Bloom, J. S., & Thompson, I. B. 2005, *ApJ*, 634, L25
- Chen, H.-W., Prochaska, J. X., & Gnedin, N. Y. 2007, *ApJ*, 667, L125
- Chen, H.-W., Prochaska, J. X., Ramirez-Ruiz, E., Bloom, J. S., Dessauges-Zavadsky, M., & Foley, R. J. 2007, *ApJ*, 663, 420
- Christensen, L., Hjorth, J., & Gorosabel, J. 2004, *A&A*, 425, 913
- Christensen, L., Wisotzki, L., Roth, M. M., Sánchez, S. F., Kelz, A., & Jahnke, K. 2007, *A&A*, 468, 587
- Cox, N. L. J., et al. 2007, *A&A*, 470, 941
- Dall'Aglio, A., Wisotzki, L., & Worsack, G. 2008, *A&A*, 491, 465
- de Ugarte Postigo, A., et al. 2010, *A&A*, 513, A42
- D'Elia, V., et al. 2007, *A&A*, 467, 629
- D'Elia, V., et al. 2009a, *ApJ*, 694, 332
- D'Elia, V., et al. 2009b, *A&A*, 503, 437
- D'Elia, V., et al. 2010, *ArXiv e-prints/1007.5357*
- Dessauges-Zavadsky, M., Chen, H.-W., Prochaska, J. X., Bloom, J. S., & Barth, A. J. 2006, *ApJ*, 648, L89
- Destree, J. D., & Snow, T. P. 2009, *ApJ*, 697, 684
- D'Odorico, S., et al. 2006, in *Society of Photo-Optical Instrumentation Engineers (SPIE) Conference*, Vol. 6269,
- Elíasdóttir, Á., et al. 2009, *ApJ*, 697, 1725
- Faucher-Giguère, C., Lidz, A., Zaldarriaga, M., & Hernquist, L. 2009, *ApJ*, 703, 1416
- Fiore, F., et al. 2005, *ApJ*, 624, 853
- Fox, A. J., Ledoux, C., Vreeswijk, P. M., Smette, A., & Jaunsen, A. O. 2008, *A&A*, 491, 189
- Frail, D. A., et al. 2001, *ApJL*, 562, L55
- Fruchter, A. S., et al. 2006, *Nature*, 441, 463
- Fynbo, J. P. U., et al. 2010, *ApJS*, 186, 485
- Fynbo, J. P. U., et al. 2009, *ApJS*, 185, 526
- Fynbo, J. P. U., et al. 2001, *A&A*, 369, 373
- Fynbo, J. P. U., Prochaska, J. X., Sommer-Larsen, J., Dessauges-Zavadsky, M., & Møller, P. 2008, *ApJ*, 683, 321
- Fynbo, J. P. U., et al. 2006, *A&A*, 451, L47
- Galama, T. J., & Wijers, R. A. M. J. 2001, *ApJ*, 549, L209
- Gehrels, N., et al. 2004, *ApJ*, 611, 1005
- Gull, T. R., Vieira, G., Bruhweiler, F., Nielsen, K. E., Verner, E., & Danks, A. 2005, *ApJ*, 620, 442
- Heckman, T. M., & Lehnert, M. D. 2000, *ApJ*, 537, 690
- Holland, S. T., et al. 2010, *ApJ*, 717, 223
- Jakobsson, P., et al. 2006a, *A&A*, 460, L13
- Jakobsson, P., Hjorth, J., Fynbo, J. P. U., Watson, D., Pedersen, K., Björnsson, G., & Gorosabel, J. 2004, *ApJ*, 617, L21
- Jakobsson, P., et al. 2006b, *A&A*, 447, 897
- Jaunsen, A. O., et al. 2008, *ApJ*, 681, 453
- Jenniskens, P., & Desert, F. 1994, *A&AS*, 106, 39
- Junkkarinen, V. T., Cohen, R. D., Beaver, E. A., Burbidge, E. M., Lyons, R. W., & Madejski, G. 2004, *ApJ*, 614, 658
- Kacprzak, G. G., Churchill, C. W., Ceverino, D., Steidel, C. C., Klypin, A., & Murphy, M. T. 2010, *ApJ*, 711, 533
- Kann, D. A., Klose, S., & Zeh, A. 2006, *ApJ*, 641, 993
- Kann, D. A., et al. 2010, *ApJ*, 720, 1513
- Krühler, T., et al. 2008, *ApJ*, 685, 376
- Lawton, B., Churchill, C. W., York, B. A., Ellison, S. L., Snow, T. P., Johnson, R. A., Ryan, S. G., & Bann, C. R. 2008, *AJ*, 136, 994
- Ledoux, C., Vreeswijk, P. M., Smette, A., Fox, A. J., Petitjean, P., Ellison, S. L., Fynbo, J. P. U., & Savaglio, S. 2009, *A&A*, 506, 661
- Levesque, E. M., et al. 2010, *MNRAS*, 401, 963
- Madau, P. 1995, *ApJ*, 441, 18
- Michałowski, M. J., Hjorth, J., Castro Cerón, J. M., & Watson, D. 2008, *ApJ*, 672, 817
- Møller, P., Fynbo, J. P. U., & Fall, S. M. 2004, *A&A*, 422, L33
- Møller, P., Warren, S. J., Fall, S. M., Fynbo, J. U., & Jakobsen, P. 2002, *ApJ*, 574, 51
- Morton, D. C. 2003, *ApJS*, 149, 205
- Murphy, M. T., & Liske, J. 2004, *MNRAS*, 354, L31
- Nestor, D. B., Johnson, B. D., Wild, V., Ménard, B., Turnshek, D. A., Rao, S., & Pettini, M. 2010, *ArXiv e-prints (1003.0693)*
- Nestor, D. B., Pettini, M., Hewett, P. C., Rao, S., & Wild, V. 2008, *MNRAS*, 390, 1670
- Nestor, D. B., Turnshek, D. A., & Rao, S. M. 2005, *ApJ*, 628, 637
- Perley, D. A., et al. 2009, *AJ*, 138, 1690
- Pettini, M., Rix, S. A., Steidel, C. C., Adelberger, K. L., Hunt, M. P., & Shapley, A. E. 2002, *ApJ*, 569, 742
- Pettini, M., Steidel, C. C., Adelberger, K. L., Dickinson, M., & Giavalisco, M. 2000, *ApJ*, 528, 96
- Pontzen, A., et al. 2010, *MNRAS*, 402, 1523
- Prochaska, J. X. 2006, *ApJ*, 650, 272
- Prochaska, J. X., Chen, H., & Bloom, J. S. 2006, *ApJ*, 648, 95
- Prochaska, J. X., et al. 2007a, *ApJS*, 168, 231
- Prochaska, J. X., Chen, H., Wolfe, A. M., Dessauges-Zavadsky, M., & Bloom, J. S. 2008a, *ApJ*, 672, 59
- Prochaska, J. X., Chen, H.-W., Dessauges-Zavadsky, M., & Bloom, J. S. 2007b, *ApJ*, 666, 267
- Prochaska, J. X., Dessauges-Zavadsky, M., Ramirez-Ruiz, E., & Chen, H. 2008b, *ApJ*, 685, 344
- Prochaska, J. X., et al. 2009, *ApJ*, 691, L27
- Pwa, T. H., & Pottasch, S. R. 1986, *A&A*, 164, 116
- Rao, S. M., Turnshek, D. A., & Nestor, D. B. 2006, *ApJ*, 636, 610
- Rau, A., et al. 2010, *ApJ*, 720, 862
- Rauch, M. 1998, *ARA&A*, 36, 267
- Rubin, K. H. R., Prochaska, J. X., Koo, D. C., Phillips, A. C., & Weiner, B. J. 2010, *ApJ*, 712, 574
- Salvaterra, R., et al. 2009, *Nature*, 461, 1258
- Savage, B. D., & Sembach, K. R. 1991, *ApJ*, 379, 245
- Savaglio, S. 2006, *New Journal of Physics*, 8, 195
- Savaglio, S., Fall, S. M., & Fiore, F. 2003, *ApJ*, 585, 638
- Savaglio, S., et al. 2004, *ApJ*, 602, 51
- Savaglio, S., Glazebrook, K., & LeBorgne, D. 2009, *ApJ*, 691, 182
- Schaefer, B. E., et al. 2003, *ApJ*, 588, 387
- Shapley, A. E., Steidel, C. C., Pettini, M., & Adelberger, K. L. 2003, *ApJ*, 588, 65
- Sheffer, Y., Prochaska, J. X., Draine, B. T., Perley, D. A., & Bloom, J. S. 2009, *ApJ*, 701, L63
- Silva, A. I., & Viegas, S. M. 2002, *MNRAS*, 329, 135
- Svensson, K. M., Levan, A. J., Tanvir, N. R., Fruchter, A. S., & Strolger, L. 2010, *MNRAS*, 479
- Tanvir, N. R., et al. 2009, *Nature*, 461, 1254
- Thöne, C. C., et al. 2010, *MNRAS Submitted*
- Thöne, C. C., Greiner, J., Savaglio, S., & Jehin, E. 2007, *ApJ*, 671, 628
- Thöne, C. C., Michałowski, M. J., Leloudas, G., Cox, N. L. J., Fynbo, J. P. U., Sollerman, J., Hjorth, J., & Vreeswijk, P. M. 2009, *ApJ*, 698, 1307
- Tumlinson, J., Prochaska, J. X., Chen, H., Dessauges-Zavadsky, M., & Bloom, J. S. 2007, *ApJ*, 668, 667
- Vreeswijk, P. M., et al. 2004, *A&A*, 419, 927
- Vreeswijk, P. M., et al. 2007, *A&A*, 468, 83
- Vreeswijk, P. M., et al. 2006, *A&A*, 447, 145
- Watson, D., et al. 2006, *ApJ*, 652, 1011
- Welty, D. E., Federman, S. R., Gredel, R., Thorburn, J. A., & Lambert, D. L. 2006, *ApJS*, 165, 138
- Wild, V., Hewett, P. C., & Pettini, M. 2006, *MNRAS*, 367, 211
- Zych, B. J., Murphy, M. T., Hewett, P. C., & Prochaska, J. X. 2009, *MNRAS*, 392, 1429

TABLE 1
WEIGHTED COMPOSITE
AFTERGLOW SPECTRUM

λ (Å)	f_λ	f_λ uncertainty
701	0.003	0.027
702	0.018	0.027
703	0.000	0.027
704	0.000	0.027
705	0.000	0.027
706	0.026	0.026
707	0.000	0.026
708	0.001	0.025
709	0.001	0.025
710	0.000	0.025
711	0.000	0.025
712	0.007	0.024
713	0.030	0.024
714	0.012	0.024

Relative flux in the composite spectrum and its associated error spectrum. This table is available in its entirety in a machine-readable form in the online journal. A portion is shown here for guidance regarding its form and content.

TABLE 2
ABSORPTION LINE LIST

Line ID	λ_{lab} (Å) ^c	λ_{obs}	W_r (Å)	notes
H I	1215.67		73	
N V	1238.82	1239.01	0.14±0.02	
N V	1242.80	1243.01	0.07±0.02	
S II	1250.58	1249.95	0.15±0.02	
S II	1253.52	1252.91	0.24±0.02	
S II	1259.52			a
Si II	1260.42	1259.95	1.26±0.02	a
Si II*	1264.74	1264.58	0.66±0.02	
C I	1277.25			
C I*	1277.28–1280.58	1277.51	0.09±0.02	blends
O I	1302.17			a
Si II	1304.37	1302.97	2.29±0.02	a
O I*	1304.86			a
Si II*	1309.28	1309.32	0.27±0.02	
Ni II	1317.22	1318.00	0.11±0.02	
C I	1328.83			a
C I*, **	1329.09–1329.60	1328.95	0.08±0.01	blends
C II	1334.53			a
C II*	1335.71	1334.99	1.73±0.02	a
Cl I	1347.24	1347.01	0.20±0.02	b
Ni II	1370.13	1370.51	0.13±0.02	
Si IV	1393.76	1393.51	0.95±0.02	
Si IV	1402.77	1402.61	0.68±0.02	
Ga II	1414.40			a, b
Ni II	1415.72	1414.95	0.16±0.02	a, b
CO	1419.0	1419.00	0.06±0.01	b
Ni II	1454.84			
Zn I	1457.57	1456.00	0.08±0.02	a, b

TABLE 2 — *Continued*

Line ID	λ_{lab} (Å) ^c	λ_{obs}	W_r (Å)	notes
CO	1477.5	1478.4	0.21±0.02	
Si II	1526.71	1526.02	0.93±0.02	
Si II*	1533.43	1533.51	0.42±0.02	
Co II	1539.47	1539.00	0.03±0.01	b
C IV	1548.20			a
C IV	1550.77	1548.33	2.18±0.03	a
C I	1560.31	1559.51	0.09±0.02	b
Fe II*	1570.25	1569.92	0.08±0.02	b
Fe II*	1602.49	1602.56	0.08±0.01	
Fe II	1608.45	1608.08	0.85±0.02	a
Fe II	1611.20	1610.81	0.18±0.02	a
Fe II*	1618.47	1618.02	0.03±0.01	a
Fe II*	1621.69	1621.60	0.11±0.02	a
Fe II*	1629.16			
Fe II*	1631.13	1629.50	0.10±0.02	a
Fe II*	1634.35			a
Fe II*	1636.33	1637.55	0.50±0.02	
Fe II*	1639.40			
C I	1656.93			
C I*, **	1656.27–1658.12	1657.02	0.14±0.02	a blends
Al II	1670.79	1670.58	1.04±0.02	
Si I	1693.29	1693.03	0.07±0.02	
Ni II	1703.41	1702.48	0.14±0.02	
Ni II	1709.60	1709.45	0.08±0.02	
Ni II	1741.55	1742.02	0.14±0.02	
Mg I	1747.79	1748.02	0.05±0.01	b
Ni II	1751.92	1752.06	0.09±0.02	
Ni II	1804.47	1805.31	0.03±0.01	a
Si I	1807.31			a
Si II	1808.01	1808.14	0.29±0.02	a
Si II*	1816.93			a, b
Si II*	1817.45	1816.95	0.12±0.01	a, b
Mg I	1827.93	1827.87	0.09±0.02	
Ni II	1842.89	1844.27	0.12±0.02	b
Al III	1854.72	1854.83	0.89±0.02	
Al III	1862.79	1863.56	0.68±0.02	
Fe I	1875.16	1874.46	0.10±0.01	a
Fe I	1883.78	1882.67	0.17±0.02	a
Si III	1892.03	1890.58	0.10±0.02	b
Fe II	1901.77	1901.36	0.14±0.02	a
Ti II	1905.77			
Ti II	1906.24	1905.99	0.11±0.02	a
Ti II	1910.75	1910.56	0.14±0.02	a
Fe I	1937.27	1938.04	0.09±0.02	a
Co II	1941.29	1941.97	0.07±0.01	a, b
Co II	2012.17	2010.99	0.06±0.02	b
Cr II	2017.57	2017.61	0.08±0.02	b
Zn II	2026.14			
Cr II	2026.27	2025.97	0.60±0.02	a
Mg I	2026.48			
Cr II	2056.26	2055.51	0.19±0.02	
Cr II	2062.23			a
Zn II	2062.66	2062.67	0.53±0.02	a

TABLE 2 — *Continued*

Line ID	λ_{lab} (Å) ^c	λ_{obs}	W_r (Å)	notes
Cr II	2066.16	2066.29	0.12±0.02	a
Ni II*	2166.23	2167.65	0.26±0.02	a
Fe I	2167.45			
Ni II*	2175.22	2175.83	0.07±0.01	
Mn I	2185.59	2186.96	0.51±0.02	
Ni II*	2217.2	2217.02	0.24±0.01	
Ni II	2223.0	2224.98	0.07±0.01	
Fe II	2249.88	2250.02	0.31±0.02	
Fe II	2260.78	2261.00	0.38±0.02	
Ni II	2316.7	2316.36	0.19±0.02	
Fe II**	2328.11	2327.65	0.10±0.02	
Fe II*	2333.52	2333.30	0.34±0.02	
Fe II	2344.21	2346.01	1.74±0.02	a
Fe II*	2345.00			
Fe II*	2349.02	2349.60	0.26±0.02	a
Fe II*	2359.83	2360.01	0.28±0.01	
Fe II*	2365.55	2365.40	0.18±0.01	
Fe II	2374.46	2374.46	1.00±0.02	
Fe II*	2381.49	2383.59	1.65±0.02	a
Fe II	2382.77			a
Fe II*	2383.79			a
Fe II*	2389.36	2389.40	0.18±0.02	a
Fe II*	2396.15	2396.50	0.71±0.02	a
Fe II*	2396.36			a
Fe II*	2399.98			a
Fe II*	2405.16	2406.04	0.40±0.02	a
Fe II*	2407.39			a
Fe II*	2411.25	2411.68	0.51±0.03	a
Fe II*	2411.80			a
Fe II*	2414.05			a
Sc II	2561.00	2562.52	0.18±0.01	a
Sc II	2563.97			a
Mn II	2576.88	2577.04	0.45±0.02	
Fe II	2586.65	2586.49	1.33±0.02	a
Mn II	2594.50	2594.36	0.45±0.02	
Fe II*	2599.15	2600.23	1.85±0.03	a
Fe II	2600.17			a
Mn II	2606.46	2607.53	0.56±0.01	a
Fe II*	2607.87			a
Fe II*	2612.65	2613.11	0.51±0.01	a
Fe II*	2614.61			
Fe II*	2618.40	2618.51	0.06±0.01	a
Fe II*	2621.19	2629.82	0.90±0.02	a
Fe II*	2622.45			a
Fe II*	2626.45			a
Fe II*	2629.08			a
Fe II*	2631.83			a
Fe II*	2632.11			a
Fe II*	2740.4	2739.45	0.07±0.01	b
Fe II*	2747.9	2749.50	0.16±0.01	b
Fe II*	2756.28	2756.50	0.08±0.01	b
Mg II	2796.35	2796.21	1.71±0.02	
Mg II	2803.53	2803.50	1.47±0.02	
Mg I	2852.96	2852.97	0.78±0.01	

TABLE 2 — *Continued*

Line ID	λ_{lab} (Å) ^c	λ_{obs}	W_r (Å)	notes
Fe I	2967.77	2966.24	0.05±0.01	b
Fe I	2984.44	2983.49	0.05±0.01	
Ti II	3073.88	3076.01	0.08±0.01	
Ti II	3242.93	3239.56	0.11±0.01	
Ti II	3384.74	3385.85	0.15±0.02	b
Ca II	3934.78	3933.97	0.76±0.02	
Ca II	3969.59	3969.98	0.66±0.02	
Ca I	4227.92	4226.93	0.11±0.02	b
Mg H	5209.45	5210.75	0.09±0.02	b

^a Lines are blended.^b Line only present in one of the two subsamples, when splitting the full sample by signal-to-noise.^c Vacuum wavelengths.TABLE 3
ABSORPTION LINE LIST BLUEWARD OF LY α

Line ID	λ_{lab} (Å)	λ_{obs} (Å)	notes
Si II	1206.500	1206.99	
N I	1199.549–1200.710	1200.47	blend
Mn II	1199.391		
Si II	1190.4158, 1193.2897	1192.96	blend
Cr*,**	1190.254–1194.686		
Cr*,**	1157.910–1160.51	1160.52	a
Fe II	1142.3656–1144.9379	1143.00	a
Cr*,**	1138.384–1141.678	1138.20	a
Fe II	1125.4478	1127.01	
Cr*,**	1121.453 - 1123.460	1121.49	a
Fe II	1081.8748		
N II	1083.990	1085.04	
Ar I	1066.660		
Fe II	1062.152–1063.9718	1066.00	
Si IV	1062.662		
Ar I	1048.2199	1049.58	
O VI	1037.6167		
C II	1036.3367	1037.55	
O VI	1031.9261	1033.00	
H I	1025.7225 (Ly β)		
Mg II	1025.9681, 1026.1134	1024.39	a
Si II	1020.6989		
Si II	1012.502	1013.04	
N II	989.799		
Si II	989.8731	989.49	
C III	977.020	979.08	
H I	972.5368	973.03	
N I	953.415, 953.655	954.49	
H I	949.7431	950.52	
H I	937.8035	937.02	
H I	930.7483	930.99	

^a Lines are blended.

TABLE 4
GRB SPECTRA CONTRIBUTING AT LYMAN LIMIT

GRB name	redshift	$\Delta\lambda_r$ (Å) ^a	S/N ($\lambda < 912.(1+z)$)	$\log N(\text{H I cm}^{-2})$ ^b
GRB 050730	3.9692	800–900	0.44	22.10±0.10
GRB 050908	3.3467	840–900	1.00	17.60±0.10
GRB 060206	4.0559	800–900	0.17	20.85±0.10
GRB 060210	3.9133	800–900	0.02	21.55±0.15
GRB 060526	3.2213	845–900	0.12	20.00±0.15
GRB 060707	3.4240	810–900	0.08	21.00±0.20
GRB 060906	3.6856	878–900	0.10	21.85±0.10
GRB 060927	5.4635	800–900	0.10	22.50±0.15
GRB 061110B	3.4344	873–900	0.52	22.35±0.10
GRB 080603	2.6892	870–900	0.12	21.85±0.05
GRB 080607	3.0368	800–900	0.04	22.70±0.15

^a Wavelength range to which each spectrum contributes to the composite blueward of the Lyman limit.

^b H I column densities are adopted from F09.

TABLE 5
COLUMN DENSITIES

Element	$\log N(\text{cm}^{-2})$ (COG)	$\log (X/H)$	$\log (X/H)_\odot$ ^a	[X/H]	$\log N(\text{cm}^{-2})$ (AOD)
H I	22.00±0.10				
C I	13.73±0.15	−8.27±0.18	−3.57		13.72±0.09
C II	16.76±0.12 ^b	−5.24±0.16		−1.55 ^c	>15.0
C IV	16.25±0.15	−5.75±0.18			>15.0
N V	13.88±0.05	−8.12±0.11	−4.17		13.90±0.10
Mg II	14.91±0.06	−7.09±0.12	−4.40	>−2.68 ^c	>14.0
Mg I	13.06±0.10	−8.94±0.14			14.20±0.15
Al II	14.80±0.20 ^d	−7.20±0.22	−5.55	−1.46 ^c	>13.4
Al III	14.54±0.20	−7.46±0.22			>14.0
Si II	16.07±0.22 ^e	−5.93±0.24	−4.49	−1.27 ^c	15.74±0.06
Si IV	15.50±0.20	−6.50±0.22			>14.1
S II	15.37±0.05	−6.63±0.11	−4.88	−1.75	15.35±0.12
Ca II	13.17±0.12 ^f	−8.83±0.16	−5.66	>−3.17	13.05±0.15
Ti II	13.03±0.25	−8.97±0.27	−7.05	−1.92	12.77±0.23
Cr II	13.77±0.05	−8.23±0.11	−6.36	−1.87	13.68±0.09
Mn II	13.56±0.08	−8.44±0.13	−6.57	−1.87	13.37±0.03
Fe II	15.70±0.07	−6.30±0.12	−4.50	−1.80 ^c	15.49±0.10
Fe I	13.50±0.15 ^g	−8.50±0.18			14.90±0.10
Co II	13.83±0.13	−8.17±0.16	−7.01	−1.16	13.73±0.21
Ni II	14.09±0.19	−7.91±0.21	−5.78	−2.13	14.22±0.21
Zn II	13.75±0.15	−8.25±0.18	−7.44	−0.81	13.64±0.04

^a Solar photosphere abundances of the neutral species of each element from Asplund et al. (2009).

^b Blended with C II* $\lambda 1335$, assuming the two lines contribute equally to the measured W_r .

^c Derived from the sum of the ionization levels. Lines are saturated, so a lower limit can be determined.

^d Determined from the single line Al II $\lambda 1670$.

^e Contaminated by Si II*.

^f The dominant species is Ca III.

^g Wide wavelength range for Fe I (1875–2984 Å). Hence the composite probe different regions, making the fit to the curve of growth bad, and values between $13.5 < \log N(\text{Fe I}) < 14.5$ are possible.